

ARTICLE



PRMT5 K240lac confers ferroptosis resistance via ALKBH5/SLC7A11 axis in colorectal cancer

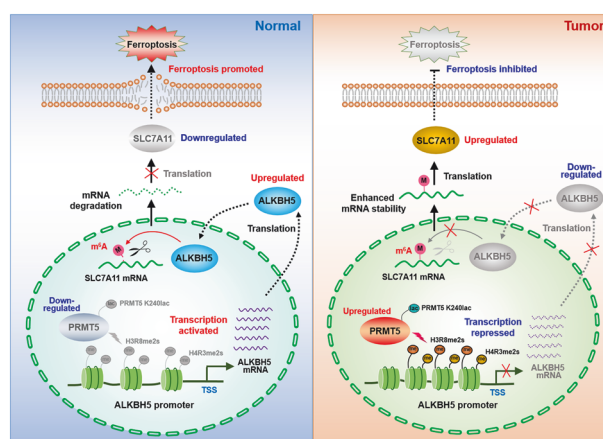
Shuang Qu^{1,11}, Baijie Feng^{2,11}, Mengying Xing^{3,11}, Yingyi Qiu^{4,11}, Longjun Ma^{5,11}, Zhou Yang⁶, Yi Ji⁷, Feng Huang⁴, Yuanrong Wang⁴, Jingwan Zhou⁴, Min Xu⁵, Jiaxin He⁴, Qinyao Zhou⁴, Xin Zhou⁴, Wenjing Xiong⁴, Bing Yao⁴, Ming Liu^{7,8}, Qiantong Dong⁹, Liu Yang¹⁰ and Shouyong Gu^{1,5}

© The Author(s), under exclusive licence to Springer Nature Limited 2025

Ferroptosis is a newly discovered type of regulated cell death, characterized by the iron-dependent accumulation of lipid reactive oxygen species, which has been implicated in a number of human diseases. However, the regulatory mechanisms underlying ferroptosis in colorectal cancer (CRC) remain unclear. In this study, we unravel the pivotal role of PRMT5 in the progression of CRC by promoting ferroptosis resistance. Mechanistically, PRMT5 directly inhibits the transcription of m⁶A demethylase ALKBH5 via histone modifications (H4R3me2s and H3R8me2s), bolstering SLC7A11 mRNA stability and expression, thereby aggravating CRC progression through attenuating ferroptosis. Particularly, our work identifies PRMT5 as a novel lactylation substrate at lysine 240 (PRMT5 K240lac), crucial for sustaining CRC ferroptosis resistance by shaping the ALKBH5/SLC7A11 axis, while mutation disrupting these effects. Overall, our work underscores the significance of PRMT5 K240lac in conferring ferroptosis resistance in CRC, proposing targeted intervention along the PRMT5 K240lac/ALKBH5/SLC7A11 axis as an innovative therapeutic approach in CRC treatment.

Oncogene; <https://doi.org/10.1038/s41388-025-03457-2>

Graphical Abstract



INTRODUCTION

Ferroptosis is a newly discovered programmed cell death characterized by iron-dependent accumulation of lethal lipid peroxidation and reactive oxygen species (ROS), which differs

morphologically and mechanistically from other forms of programmed cell death, including apoptosis, necroptosis, pyroptosis and autophagic cell death [1]. A number of cellular variables have been implicated in the control of ferroptosis, such as iron content,

¹Geriatric Hospital of Nanjing Medical University, Nanjing, Jiangsu, China. ²Department of Medical Oncology, Shanghai Pudong Hospital, Fudan University Pudong Medical Center, Shanghai, China. ³The State Key Laboratory of Pharmaceutical Biotechnology, School of Life Sciences, Nanjing University, Nanjing, China. ⁴National Experimental Teaching Center of Basic Medical Science, School of Basic Medical Sciences, Nanjing Medical University, Nanjing, China. ⁵Department of Epidemiology, School of Public Health, Nanjing Medical University, Nanjing, China. ⁶Department of Head and Neck Surgery, Fudan University Shanghai Cancer Center, Shanghai, China. ⁷Affiliated Hospital of Integrated Traditional Chinese and Western Medicine, Nanjing University of Chinese Medicine, Nanjing, China. ⁸The Third Clinical Medical College, Nanjing University of Chinese Medicine, Nanjing, China. ⁹Department of Gastrointestinal Surgery, The First Affiliated Hospital of Wenzhou Medical University, Wenzhou, China. ¹⁰Department of Colorectal Surgery, The Affiliated Cancer Hospital of Nanjing Medical University & Jiangsu Cancer Hospital & Jiangsu Institute of Cancer Research, Nanjing, China. ¹¹These authors contributed equally: Shuang Qu, Baijie Feng, Mengying Xing, Yingyi Qiu, Longjun Ma. ✉email: lium@njucm.edu.cn; dongqt2021@wmu.edu.cn; yangliu@njmu.edu.cn; gushouyong@jspggh.com

Received: 6 January 2025 Revised: 7 May 2025 Accepted: 19 May 2025

Published online: 30 May 2025

amino acid uptake, dysregulation of mitochondrial metabolism, decrease of cellular antioxidant capacity, accumulation of lipid ROS and glutathione biosynthesis [2]. Emerging evidence shows that ferroptosis is closely associated with the regulation of a diverse array of pathophysiological processes, including metabolic diseases [3], nervous system disorders [4], cardiovascular disease [5], injury of different tissues and organs [6, 7], inflammation [8], atherogenesis [9], diabetes and cancer [10, 11]. In recent years, ferroptosis has sparked an explosion of research in the field of oncology, as targeting ferroptosis might hold great promise and potential for treating cancers that are refractory or intolerant to conventional therapies [12, 13].

Post-translational modifications (PTMs), which refer to the covalent additions of functional groups (e.g., methyl, acetyl, phosphate, ubiquitin, and glycan) to amino acid residues, significantly affect the physical, chemical, and biological properties of proteins in eukaryotic cells [14, 15]. PTMs are particularly important and govern a broad array of biological processes, such as gene transcription [16], DNA replication [17], DNA damage repair [18], modulation of protein activity and stability [19], heterochromatin formation and maintenance [20], mRNA splicing [21], and mitosis [22]. As a prevalent PTM, protein arginine methylation is catalyzed by a family of enzymes called protein arginine methyltransferases (PRMTs), which catalyze the transfer of the methyl group from S-adenosyl-L-methionine (AdoMet) to the guanidino nitrogen atoms of arginine residues of protein substrates [23]. As a predominant type II protein arginine methyltransferase, PRMT5 can catalyze the formation of symmetric di-methylation of arginine residues on histone H4 (H4R3me2s), H3 (H3R8me2s) and H2A (H2AR3me2s), which are closely associated with transcriptional inactivation [24].

PRMT5-mediated methylation of protein substrates is involved in regulation of a broad range of biological processes under normal and pathological conditions, including pre-mRNA splicing, transcription initiation and elongation, translation, and ribosome biogenesis [25]. Emerging evidence reveals that PRMT5 is aberrantly expressed in a wide spectrum of cancers, such as acute leukemia, lymphoma and breast cancer, and exerts important functions involved in tumorigenesis, progression, and metastasis by facilitating cell proliferation, invasion and migration [26]. Thus, targeting PRMT5 is becoming a promising and valuable therapeutic strategy in the treatment of cancers, especially in CRC [27]. However, the functional impact and potential mechanisms of PRMT5 in ferroptosis are still unclear and need to be further explored.

Lactate has long been misunderstood as a “dead-end” waste by-product of anaerobic glycolysis. In 2019, Professor Yingming Zhao’s research group proposed for the first time that lactate can drive the formation of lactylated lysine residues (Kla) on histone H3, H4, H2A and H2B in human and mouse cells, which function as epigenetic marks that directly control gene transcription [28]. Inspired by this discovery, a growing number of studies on protein lactylation have emerged in recent years [29]. Many other histone and non-histone Kla sites have been identified in a wide range of physiological and pathological conditions, including cell fate determination, inflammation, fibrosis, embryonic development, and gene transcription [30]. Protein lactylation thus provides an opportunity to greatly expand our understanding of its biological effects and potential mechanisms in diverse pathophysiological conditions, especially in cancer.

Here, we found that PRMT5 promotes ferroptosis resistance of CRC cells via the ALKBH5/SLC7A11 axis. PRMT5 directly inhibits the expression of ALKBH5 at the transcriptional level via repressive histone modifications H4R3me2s and H3R8me2s, which contributes the stability of SLC7A11 mRNA and further facilitates the expression of SLC7A11, thereby driving CRC progression through promoting ferroptosis resistance. More importantly, PRMT5 was identified as a lactylation substrate, and lactylation of PRMT5 at

K240 (PRMT5 K240Iac) is essential for PRMT5 to modulate ALKBH5/SLC7A11 axis and promote ferroptosis resistance of CRC cells. Collectively, this study emphasizes the importance of PRMT5 K240Iac/ALKBH5/SLC7A11 axis in conferring ferroptosis resistance of CRC cells.

MATERIALS AND METHODS

Specimen

A total of 80 patients with CRC were recruited for this study with an average age of 65.8. Surgical specimen from diagnosis and surgery were reviewed and confirmed by two independent pathologists. The study protocol was approved by the local Ethics Committee of the Jiangsu Province Geriatric Hospital, and written informed consent was obtained from all participants. To conduct Kaplan-Meier survival analysis, a tissue microarray containing 90 pairs of CRC and matched adjacent normal samples was purchased from Shanghai Outdo Biotech company (HCO-IA180Su18; Shanghai, China), which includes a survival update at a follow-up of >5 years for patients with CRC.

Cell lines, culture conditions and transfection

Human CRC cell lines HCT116, CoCa-2, SW620, SW480, HCT-15 and LoVo, as well as human fetal colonic epithelial cell line FHC and embryonic kidney cell line HEK-293T, were obtained from the Cell Bank of Type Culture Collection of Chinese Academy of Sciences (Shanghai, China) or American Type Culture Collection (ATCC). HCT116 cells were cultured in McCoy’s 5A (16600082; Gibco). HCT-15 and FHC cells were cultured in RPMI 1640 (11875093; Gibco). SW620 and SW480 cells were cultured in L-15 (11415064; Gibco). LoVo cells were cultured in F-12K (21127022; Gibco). FHC and HEK-293T cells were cultured in Dulbecco’s modified Eagle’s medium (10566016; Gibco). All cultures were supplemented with 10% (v/v) fetal bovine serum (FBS; ExCell Bio) and 1% (v/v) penicillin-streptomycin (C0222; Beyotime) at 37 °C in a humidified atmosphere containing 5% CO₂. Chemically synthesized siRNAs or plasmids were transfected into cells by Lipofectamine™ 3000 transfection reagent (L3000150; Invitrogen) according to the manufacturer’s instructions. The sequences of siRNAs or shRNA were shown in Table S2.

Establishment of stable cell lines

Lentivirus particles were generated using pLKO and pLVX vectors to stably silence or overexpress the indicated genes. pLKO, psPAX2 and pMD2.G three-packaging system was used for obtaining silencing-expression viruses, and pLVX, psPAX2 and pMD2.G three-packaging system was used for generating high-expression viruses. The constructed lentivirus plasmid backbone and packaging plasmids psPAX2 and pMD2.G were co-transfected into HEK-293T cells. The lentivirus-containing supernatants were collected and filtered through cellulose acetate membranes (pore size: 0.22 µm; Millipore) at 48 h after transfection. CRC cells were infected by the lentivirus and screened with puromycin (540222; Sigma-Aldrich) at a concentration of 1–2 µg/mL for 4–7 days. The expression levels of the indicated genes in the lentivirus-infected cells were confirmed by qRT-PCR and Western blotting.

RNA isolation and quantitative real-time PCR (qRT-PCR)

Total RNA was extracted from CRC cells or tissues by using RNA isolater Total RNA Extraction Reagent (R401-01; Vazyme) according to the protocol provided by the manufacturer. RNA quality, purity and integrity were assessed with the NanoDrop ND-1000 spectrophotometer (Thermo Scientific) and BioAnalyzer 2100 (Agilent Technologies), respectively. Equal amounts of RNA (1 µg) were reversely transcribed into cDNA using the HiScript II Reverse Transcriptase (R212-01; Vazyme). Subsequently, qRT-PCR analyses were performed for duplicated samples on a CFX96 Real-Time PCR detection system (BioRad) by using the AceQ qPCR SYBR Green Master Mix (Q121-02; Vazyme). Quantification was standardized to glyceraldehyde-3-phosphate dehydrogenase (GAPDH), and relative mRNA abundance was calculated by the $2^{-\Delta\Delta C_t}$ method. Specific primers designed for qRT-PCR were provided in Table S3.

Protein extraction and Western blotting

Cells were washed twice with ice-cold PBS and lysed with Cell Lysis Buffer (P0013; Beyotime) supplemented with protease and phosphatase inhibitor cocktail (P1048; Beyotime) for 30 min on ice. The lysates were centrifuged

at $14,000 \times g$ for 10 min at 4°C , and then the protein concentration was measured by a BCA Protein Assay Kit (P00125; Beyotime). After boiling at 100°C for 5 min in sample loading buffer (P0015; Beyotime), the protein extracts were electrophoresed in 8–15% sodium dodecyl sulfate—polyacrylamide gel electrophoresis (SDS-PAGE) gels and transferred to polyvinylidene difluoride (3010040001; Roche) membranes using a semi-dry transfer apparatus (Bio-Rad). The membranes were incubated with 5% (w/v) non-fat milk for 1–2 h at room temperature, and then incubated with primary antibodies overnight at 4°C . After incubation with horseradish peroxidase (HRP)-conjugated secondary antibodies for 1–2 h, immunoreactive proteins were visualized using a Tanon™ Femto-sig ECL kit (180–506; Tanon).

Co-Immunoprecipitation (Co-IP)

Cells were washed and lysed with Cell Lysis Buffer (P0013; Beyotime) supplemented with protease and phosphatase inhibitor cocktail (P1048; Beyotime) for 30 min on ice. After centrifugation for 10 min at $14,000 \times g$, the clear supernatant (100 μL) containing the soluble proteins was incubated with 2.5 μg of primary or control IgG antibodies and Protein A/G Magnetic beads (PB101; Vazyme) overnight at 4°C with continual rotation. After washing with lysis buffer, the precipitate was boiled with sample loading buffer (P0015; Beyotime) for 5 min and subjected to Western blotting analysis using appropriate antibodies.

LC-MS/MS analysis and database search

Highly sensitive mass spectrometry analysis (LC-MS/MS) of lactylated proteins was performed by Jingjie PTM Biolabs (Hangzhou, China) according to a previous report [31]. Briefly, the sample was digested overnight by trypsin and the resulting tryptic peptides were incubated with pre-washed Anti-L-lactyllysine antibody conjugated agarose beads (PTM-1404; PTM Bio) at 4°C overnight with continual rotation. After washing with NETN buffer (100 mM NaCl, 1 mM EDTA, 50 mM Tris-HCl, 0.5% NP-40, pH 8.0), the tryptic peptides were eluted from the agarose beads with 0.1% trifluoroacetic acid and concentrated with C18 ZipTips (ZTC18M; Millipore). The peptides were separated using a nanoElute ultra-high performance liquid chromatography (UHPLC) system and subjected to MS analysis using a timsTOF Pro instrument (Bruker Daltonics). The acquired raw data were analyzed using the MaxQuant program (v.1.6.15.0). Quantitative analysis of the relative values of lactylated peptides were performed by centralizing the signal intensity levels across samples. All resulting ratios of lactylated peptides were normalized to their corresponding protein expression levels.

Cleavage Under Target & Tagmentation (CUT&Tag)

CUT&Tag was conducted by using the Hyperactive Universal CUT&Tag Assay Kit for Illumina (TD903-01; Vazyme) following the manufacturer's instructions. Briefly, HCT116 cells were collected, bound to Concanavalin A covalently linked magnetic beads (N515-01; Vazyme), digitonin-permeabilized, and incubated with H4R3me2s (61988; Active Motif) or H3R8me2s (PTM-672; PTM Bio) antibodies. After incubation with hyperactive pAG-Tn5 Transposase (S604-01; Vazyme), the DNA was extracted, PCR-amplified and purified. The prepared DNA library was sequenced using the NovaSeq 150PE platform (Illumina, San Diego, CA, USA).

Cell viability assay

Cell viability was assessed using a Cell Counting Kit-8 (CCK-8; A311-01; Vazyme) assay. Cells were seeded in 96-well plates at a density of 3×10^3 cells per well and cultured in complete medium for 24 h at 37°C in a humidified 5% CO_2 atmosphere. At the indicated times (0, 24, 48, 72 and 96 h), 10 μL of the CCK-8 reagent was added to each well. 2 h later, the absorbance of each well was measured at a wavelength of 450 nm (OD450) using a microplate reader (Bio-Rad).

Colony-formation assay

Cells were implanted into 12-well plates and cultured in medium containing 10% (v/v) FBS and 1% (v/v) penicillin-streptomycin at 37°C in a humidified 5% CO_2 incubator. Two weeks later, colonies were fixed with 4% Paraformaldehyde Fix Solution (P0099; Beyotime) for 30 min, and then stained with Crystal Violet Staining Solution (C0121; Beyotime) for 30 min at room temperature. After washing, the colonies (≥ 50 cells) were counted to assess colony forming efficiency under a microscope (Olympus Corporation).

RNA stability assay

Cells were seeded in the 6-well plates and exposed to 5 $\mu\text{g}/\text{mL}$ Actinomycin D (SBR00013; Sigma-Aldrich) for 0, 2, 4 and 6 h at 37°C in a humidified 5% CO_2 incubator. RNA was isolated at the indicated times, reverse-transcribed and analyzed by qRT-PCR assays.

RNA immunoprecipitation (RIP) assay

Cells were washed, harvested and re-suspended in RIPA lysis buffer containing a protease inhibitor cocktail and RNase inhibitor (P0013; Beyotime). After centrifuging at 13,000 rpm for 10 min at 4°C , the supernatant was incubated with 40–50 μL precleared protein A/G beads (B23202; Bimake) and 2.5 μg anti-ALKBH5 (16837-1-AP; ProteinTech) or anti-IgG (30000-0-AP; ProteinTech) antibodies for 4 h at 4°C with gentle rotation. After washing with RIPA lysis buffer, the beads were incubated with Proteinase K (ST535; Beyotime) using Trizol reagent (15596018CN; Invitrogen). Subsequently, the mRNA expression level of SLC7A11 was analyzed by qRT-PCR and normalized to the input samples.

Measurement of lipid ROS levels

The lipid ROS level was measured by C11-BODIPY 581/591 (RM02821; ABclonal) according to the manufacturer's instructions. Briefly, C11-BODIPY 581/591 was dissolved in dimethyl sulfoxide and diluted with 10 mM HEPES buffer (pH 7.2; Sigma-Aldrich). Cells were incubated with 5 μM C11-BODIPY 581/591 for 30 min at 37°C . After washing with PBS, cells were digested and re-suspended in PBS supplemented with 5% FBS, then analyzed on a flow cytometer (BD Biosciences). To determine the lipid ROS levels in tissues, single-cell tissue suspensions were prepared using collagenase IV (C4-BIOC; Sigma-Aldrich) and hyaluronidase (ST1384; Beyotime), and then proceeded as described above. All acquired data were analyzed using FlowJo software v10.0 (TreeStar Inc., Ashland, OR, USA).

Malondialdehyde (MDA) assay

The MDA levels in cells and tissues were determined using an MDA detection kit (S0131; Beyotime) according to the manufacturer's instructions.

Iron measurement

For flow cytometric analysis of cellular iron, cells were seeded in six-well plates at a density of 5×10^5 cells per well. 24 h later, cells were washed with PBS, suspended in a serum-free medium, and incubated with 0.5 μM of fluorescent probe Mito-FerroGreen (M489; Dojindo) for 30 min at 37°C . Cellular Fe^{2+} was analyzed using a flow cytometer (BD Biosciences) under PE channel, and data were analyzed using FlowJo software v10.0.

Fluorescence staining of cellular iron

Cells were seeded on microscope cover glass in six-well plates for 24 h, stained with Mito-FerroGreen (1 μM) for 30 min at 37°C in a 5% CO_2 incubator, and imaged using an inverted confocal laser scanning microscope equipped with a $60 \times$ oil immersion optic (Leica, TCS SP8).

Transmission electron microscope (TEM)

Cells were washed with $1 \times$ PBS, fixed with 2.5% glutaraldehyde in 0.1 M phosphate buffer (pH 7.4), and then treated with 1% OsO_4 for 2 h. After dehydration with a graded alcohol series, the cells were embedded in epoxy resin (Epon 812), cut into ultra-thin sections, and subsequently stained with uranyl acetate and lead citrate. The morphology of mitochondria was imaged with an HT7700-SS transmission electron microscope (Hitachi, Tokyo, Japan).

Chromatin immunoprecipitation (ChIP)

ChIP assay was performed essentially as described previously by using a ChIP Assay Kit (P2078; Beyotime). 5×10^6 cells were cross-linked with 1% formaldehyde for 5 min at 37°C and quenched with 0.125 M glycine solution for 5 min at room temperature. Cells were washed twice with ice-cold PBS containing phenylmethanesulfonyl fluoride (PMSF; ST506; Beyotime), suspended in SDS lysis buffer and sonicated by a BIORUP-TOR®Plus (Diagenode; 20 times, 30 s on/90 s off) to yield chromatin fragments (200–500 bp). The lysates were then incubated with Protein A/G Agarose/Salmon Sperm DNA suspension and antibodies (anti-H4R3me2s, anti-H3R8me2s or control IgG) overnight at 4°C . The immunoprecipitated

complexes were gently salt-washed with Low Salt Immune Complex Wash Buffer, High Salt Immune Complex Wash Buffer, LiCl Immune Complex Wash Buffer and TE Buffer for 5 min at 4°C, respectively. The washed immunoprecipitated protein-DNA complexes were eluted with Elution Buffer, de-crosslinked by 0.2 M NaCl overnight at 65°C, and digested with Proteinase K (1073930010; Sigma-Aldrich) for 1 h at 45°C. Finally, the DNA was purified by a DNA Purification Kit (D0033; Beyotime). The primer sequences for ChIP-qPCR were listed in Table S4.

Hematoxylin and eosin (H&E) staining

Sections were dewaxed with xylene and rehydrated through a graded alcohol series (70–100%). After washing with ddH₂O, the sections were stained with H&E stain (Beyotime; C01055) for 5–10 min at room temperature. Then, sections were rinsed with ddH₂O, dehydrated through alcohol and xylene, and cover-slipped with a permanent mounting medium.

Immunohistochemistry (IHC) staining

Tissue samples were fixed in 10% neutral buffered formalin (BL539A; Shanghai Universal Biotech), embedded in paraffin and sectioned into 4-μm-thick sections with a microtome (Leitz, Germany). Tissue sections were deparaffinized in xylene, hydrated in a descending ethanol gradient and rinsed three times with PBS. Antigen retrieval was performed by boiling the slides in citrate antigen retrieval solution (pH 6.0; P0081; Beyotime) at 100°C for 15 min. Nonspecific binding sites were blocked with 10% goat serum (C0265; Beyotime) for 30 min at room temperature. The slides were then incubated with primary antibodies for 1 h at room temperature, including anti-PRMT5 (1:200; 18436-1-AP; ProteinTech), anti-H4R3me2s (1:200; 61988; Active Motif), anti-H3R8me2s (1:200; PTM-672; PTM Bio), anti-ALKBH5 (1:200; 16837-1-AP; ProteinTech), anti-SLC7A11 (1:100; 26864-1-AP; ProteinTech) and anti-Ki-67 (1:1000; 27309-1-AP; ProteinTech). After washing, the slides were incubated with HRP-labeled Goat Anti-Rabbit IgG (1:50; A0208; Beyotime) for 60 min, immunostained by 3,3'-diaminobenzidine tetra-hydrochloride (P0202; Beyotime), and counterstained by 2-(4-Aminodiphenyl)-6-indolecarbamidine dihydrochloride (C1002; Beyotime) to visualize nuclei. The positive signals of the immunostained slides were observed under a microscope (Olympus Corporation). Semi-quantitative histologic score (H score: range 0–300) was calculated for each patient according to the original formula: H score = $\sum \pi(i+1)$, where “i” is the intensity score (0–3) and “pi” is the percentage of immunostained cells for each given intensity.

Animal experiments

Immunodeficient BALB/c nude mice (Male, 6 weeks old) were used to establish xenograft models. The mice were allowed free access to food and water, and housed in cages at a controlled temperature (22 ± 2°C) and relative humidity (55 ± 5%) in a standardized 12-h light/dark cycle. HCT116 cells were harvested by centrifugation, washed with PBS and suspended in ice-cold 10% Matrigel (354234; Corning) at a density of 2×10^7 cells/mL. 2×10^6 cells (100 μL) were injected subcutaneously into the right flank of each mouse for tumor formation. When tumors reached a volume of ~50 mm³, mice were daily injected intraperitoneally with Erastin (25 mg/kg; HY-15763; MCE) or Fer-1 (2 mg/kg; HY-100579; MCE). Tumor dimensions were measured and recorded every 5 days using a digital caliper, and tumor volume (V) was calculated using the formula: $V = 0.5 \times \text{length} \times \text{width}^2$. At the end of the experiment, all mice were sacrificed, and the tumor tissues were immediately excised and weighed.

Azoxymethane/dextran sodium sulfate (AOM/DSS)-induced CRC mouse model was proposed to investigate the role of PRMT5 in controlling CRC development. One week before experiments, adenoviruses expressing murine PRMT5 shRNA (sh-PRMT5) or control (NC) were administered by enema. C57BL/6J-Apc^{Min/+} mice were intraperitoneally injected with 12 mg/kg of AOM (A5486; Sigma). After 4 days, mice were fed with drinking water containing 2% (w/v) DSS (9011-18-1; MP Biomedicals) for 5 consecutive days (repeated thrice). On day 60, mice were sacrificed, and their colonic tissues were collected for further analysis. All animal experiments were reviewed and approved by the Animal Experiment Ethics Committee of Jiangsu Province Geriatric Hospital.

Data acquisition and processing

ChIP-seq datasets in HCT116 cells were downloaded from NCBI GEO database, including H3K4me1 (GSM2711385), H3K4me2 (GSM2711391), H3K4me3 (GSM2916031) and H3K27ac (GSM2916001), and RNA

polymerase II (RNA Pol II; GSM2916013), H3K9me2 (GSM2916019) and H3K27me3 (GSM2916037). The RNA sequencing results of primary CRC samples were downloaded from GSE17538 (19914252; n = 238) and GSE39582 (23700391; n = 585). Genes used to calculate the ferroptosis related scores via AddModuleScore command were accessed from the FerrDb website (36305834). We utilized GSVA command in R package GSVA (23323831) to calculate the signature score, with calculating method set to ssGSEA. The CRISPR score (DepMap Public 24Q2 + Score, Chronos) were obtained from the DepMap portal website. A lower CRISPR score represented higher essentiality of a specific gene in a given cell line. The well annotated single-cell RNA-seq data were obtained from a previous study, which contained 25 Korean and 6 Belgian treatment-naïve patients diagnosed with CRC (32451460). To elucidate the correlation of PRMT5 with ferroptosis with higher accuracy, cells with similar K-nn graph partitions were divided into small (~20–200 typically) homogeneous groups called metacells for comparison (31604482). The metacells were generated by Scimply command. The gene expression data was calculated by supercell_GE command, reflecting the average value of a specific gene within one metacell.

Statistical analysis

All statistical analyses were performed using SPSS 18.0 (IBM, Armonk, NY) and GraphPad Prism 8.0 (GraphPad, CA, USA). All results are expressed as mean values ± standard deviation (SD) from three independent experiments. Differences between the two groups were analyzed using Student's *t*-test. Spearman correlation analysis was performed to evaluate the relationships between variables. *P* value less than 0.05 was considered statistically significant. The statistical significance was set at **P* < 0.05 and ***P* < 0.01.

RESULTS

PRMT5 is required for the proliferation of CRC cells and negatively associated with ferroptosis in CRC

PRMT5 is a type II protein arginine methyltransferase that has been implicated in the development and progression of various types of human cancers, including CRC [26, 32]. We raised the question whether PRMT5 influences the proliferation capacity of CRC cells. PRMT5-silenced HCT116 and LoVo cells were established by using siRNAs, and CCK-8 and colony-formation assays showed that PRMT5 inhibition significantly decreased the proliferative activities of HCT116 and LoVo cells (Fig. 1A, B). Subsequently, we investigated whether PRMT5 is involved in CRC pathogenesis using AOM/DSS-induced CRC model mice. We observed that PRMT5-deficient Apc^{Min/+} mice (sh-PRMT5) developed significantly fewer and smaller tumors than that in control Apc^{Min/+} mice (Fig. 1C, D). The tumors were histologically examined by H&E staining, and decreased levels of PRMT5 and Ki-67 were observed in sh-PRMT5 colon tissues by IHC staining (Fig. 1E, F). In conclusion, these data therefore suggest that PRMT5 functions as an oncogene in CRC through promoting cell proliferation in vitro and in vivo.

Previous reports have uncovered that the inhibition of ferroptosis is closely related to CRC progression [33]. To investigate whether the proliferation-promoting effect of PRMT5 on CRC cells is due to inhibition of ferroptosis, we collected 24 pairs of fresh CRC and adjacent non-cancerous tissues. We confirmed the upregulation of PRMT5 in these CRC tissues by IHC staining and qRT-PCR assays (Fig. 1G–I). The degree of ferroptosis was measured by detecting the level of ferroptosis-related indicator-lipid ROS. The result showed that lipid ROS level was significantly decreased in CRC tissues, suggesting that ferroptosis was inhibited in CRC (Fig. 1J). The protein or mRNA levels of PRMT5 were analyzed in CRC tissues from high and low lipid ROS groups, and the results showed that PRMT5 expression decreased as lipid ROS level increased (Fig. 1K, L). To further verify the relationship between PRMT5 and ferroptosis, CCK-8 assay was performed to evaluate the effect of PRMT5 knockdown on the cell viability of HCT116 and LoVo cells treated with different concentrations of ferroptosis inducers (Erastin or RSL3). We observed that siRNAs-mediated knockdown of PRMT5 significantly aggravated Erastin- and RSL3-induced ferroptotic cell death

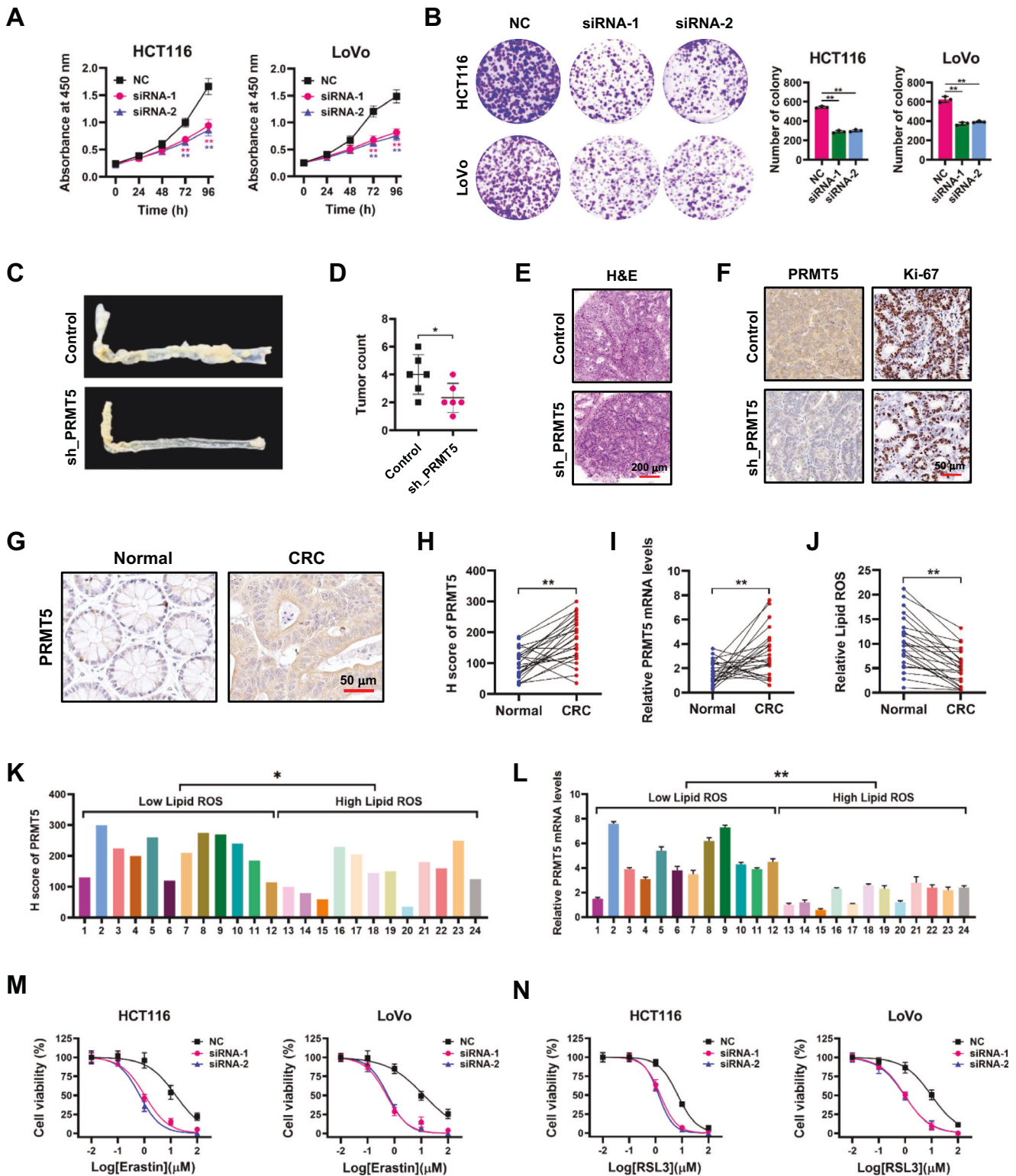
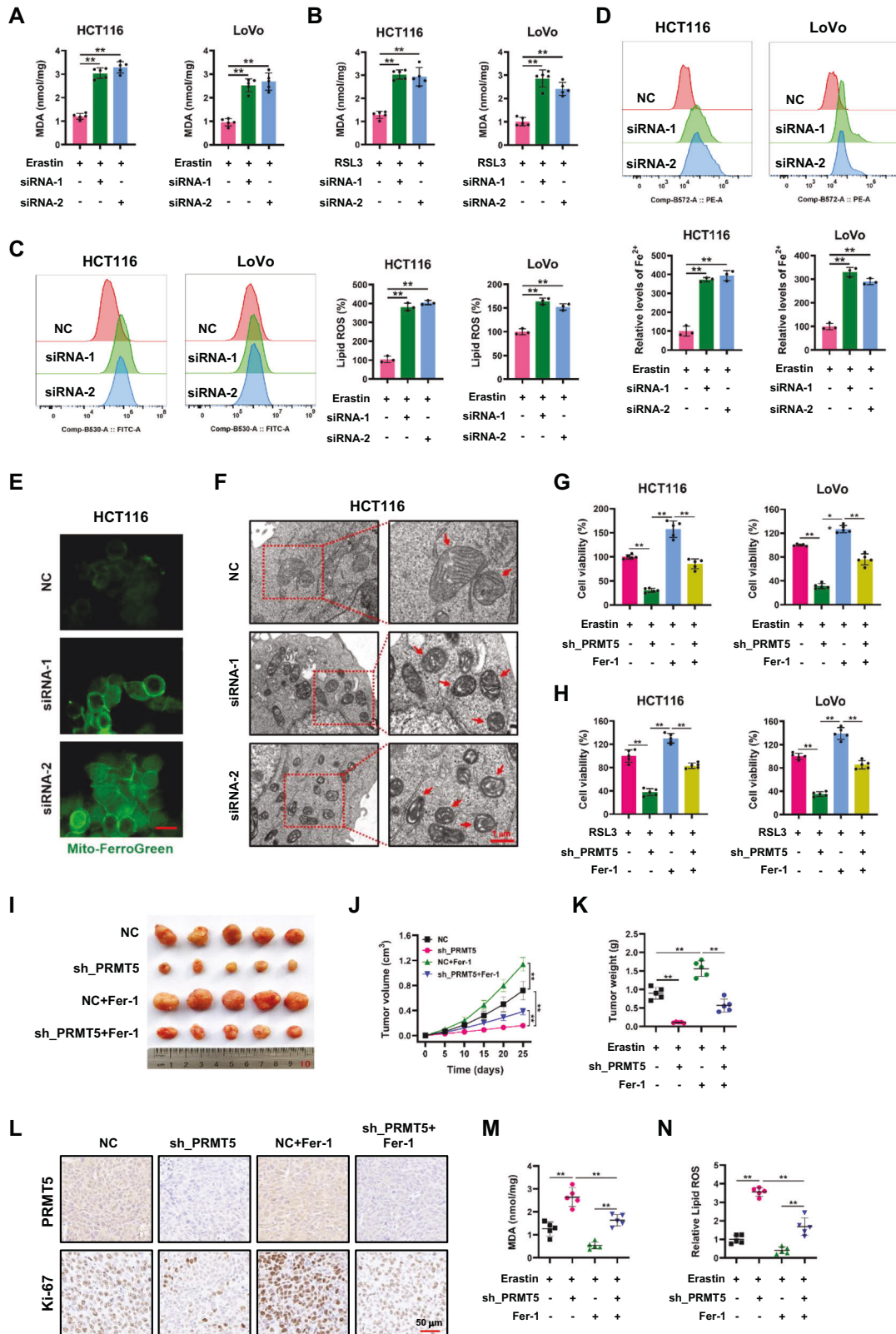


Fig. 1 PRMT5 is required for the proliferation of CRC cells and negatively associated with ferroptosis in CRC. **A, B** CCK-8 and colony-formation assays were performed to evaluate the effect of PRMT5 knockdown on the proliferation of HCT116 and LoVo cells. **C** Representative images of the colon tumors in sh_PRMT5 and control mice. **D** The tumor number in sh_PRMT5 and control mice was analyzed. **E, F** H&E and IHC staining of PRMT5 and Ki-67 in tumor sections of sh_PRMT5 and control mice. Scale bars, 200 μ m or 50 μ m. **G, H** IHC staining and H score of PRMT5 in 24 pairs of CRC and adjacent normal tissues. Scale bar, 50 μ m. **I** Relative mRNA levels of PRMT5 in 24 pairs of CRC and adjacent normal tissues. **J** Relative lipid ROS levels in CRC and adjacent normal tissues (n = 24). **K** H scores of PRMT5 in CRC tissues with low (n = 12) and high (n = 12) levels of lipid ROS. **L** Relative mRNA levels of PRMT5 in CRC tissues with low (n = 12) and high (n = 12) levels of lipid ROS. **M, N** Cell viability was measured by CCK-8 assay in NC and PRMT5-depleted HCT116 and LoVo cells treated with the indicated doses of Erastin and RSL3. The data shown represent the mean \pm SD. * P < 0.05, ** P < 0.01.



(Fig. 1M, N). Collectively, these data suggested that PRMT5 is negatively associated with ferroptosis in CRC.

Consistently, we evaluated the correlation between 9 protein arginine methylation related genes and ferroptosis related signatures based on the single-cell RNA-seq results from two

large CRC cohorts (Fig. S1A). Judging from the common results from the two cohorts, CARM1, PRMT1, PRMT2 and PRMT5 were positively correlated with ferroptosis suppressor signatures, while PRMT5 also showed negative correlation with ferroptosis marker in the GSE17538 cohort. Further analysis of CRISPR score indicated

Fig. 2 Knockdown of PRMT5 promotes ferroptosis in vitro and in vivo. **A, B** MDA levels were measured in NC or PRMT5 siRNAs-transfected HCT116 and LoVo cells treated with 2.5 μ M Erastin or 5 μ M RSL3. **C** Lipid ROS and **D** Fe^{2+} levels were analyzed by flow cytometry in NC or PRMT5 siRNAs-transfected HCT116 and LoVo cells treated with 2.5 μ M Erastin. **E** Fluorescence staining of ferrous ion was detected with Mito-FerroGreen dye in NC or PRMT5 siRNAs-transfected HCT116 cells treated with 2.5 μ M Erastin. Scale bar, 25 μ m. **F** TEM images of NC or PRMT5 siRNAs-transfected HCT116 cells treated with 2.5 μ M Erastin. Red arrows indicate mitochondria in cells. Scale bar, 1 μ m. **G, H** Cell viability was measured by CCK-8 assay in control and PRMT5-depleted (sh_PRMT5) HCT116 and LoVo cells treated with 2.5 μ M Erastin or 5 μ M RSL3 and 1 μ M Fer-1. **I** Image of subcutaneous xenografts derived from control and sh_PRMT5 nude mice treated with Erastin or Fer-1. **J, K** Tumor volumes and weights of different groups were measured. **L** Representative IHC images of PRMT5 and Ki-67 in different groups. Scale bar, 50 μ m. **M, N** MDA and Lipid ROS levels in different groups were measured. The data shown represent the mean \pm SD. $^{**}P < 0.01$.

that PRMT5 had the second lowest CRISPR score, indicating that PRMT5 was also essential for survival of CRC cell lines (Fig. S1B). Three independent single-cell RNA-seq, which were well annotated into 6 major cell types, were applied to further validate the correlation of PRMT5 with ferroptosis related signatures. (Fig. S1C). We observed that PRMT5 was expressed in annotated epithelial cells from the tumor or border area (Fig. S1D). Subsequently, these tumor cells were simplified into meta-cells (Fig. S1E), and the spearman correlation results revealed that PRMT5 expression was positively correlated with ferroptosis suppressor marker score (Fig. S1F), and was negatively correlated with ferroptosis marker score (Fig. S1G), indicating the ferroptosis-prohibiting role of PRMT5 in CRC.

Knockdown of PRMT5 accelerates ferroptosis of CRC cells in vitro and in vivo

CCK-8 and colony-formation assays were performed to confirm the role of PRMT5 in Erastin- or RSL3-induced ferroptosis of HCT116 and LoVo cells. We observed that siRNAs-mediated knockdown of PRMT5 significantly facilitated the ferroptosis of HCT116 and LoVo cells (Fig. S2A–C). Subsequently, we determined the MDA and lipid ROS levels in HCT116 and LoVo cells with PRMT5 knockdown by siRNAs. As anticipated, we found that PRMT5 knockdown significantly increased the MDA and lipid ROS levels in CRC cells treated with Erastin or RSL3 (Fig. 2A–C). In addition, the concentration of Fe^{2+} in PRMT5-depleted HCT116 and LoVo cells was significantly increased as compared to negative controls (Fig. 2D). Consistently, fluorescence staining of mitochondria with Mito-FerroGreen dye apparently showed reinforced brightness of green fluorescence in PRMT5-deficient HCT116 cells (Fig. 2E). Because ferroptosis has morphological features of mitochondria that are distinct from other forms of cell death, transmission electron microscope (TEM) was used to observe the morphologic changes of mitochondria in HCT116 cells. We observed that the cells exhibited shrunken mitochondria with enhanced membrane density after PRMT5 knockdown, a typical morphologic feature of ferroptosis (Fig. 2F). Ferrostatin-1 (Fer-1), a ferroptosis inhibitor, was used to check whether PRMT5 can inhibit ferroptosis. Interestingly, we observed that PRMT5 knockdown significantly aggravated cell death by Erastin or RSL3, and cell death could be rescued by Fer-1 (Fig. 2G, H and Fig. S2D).

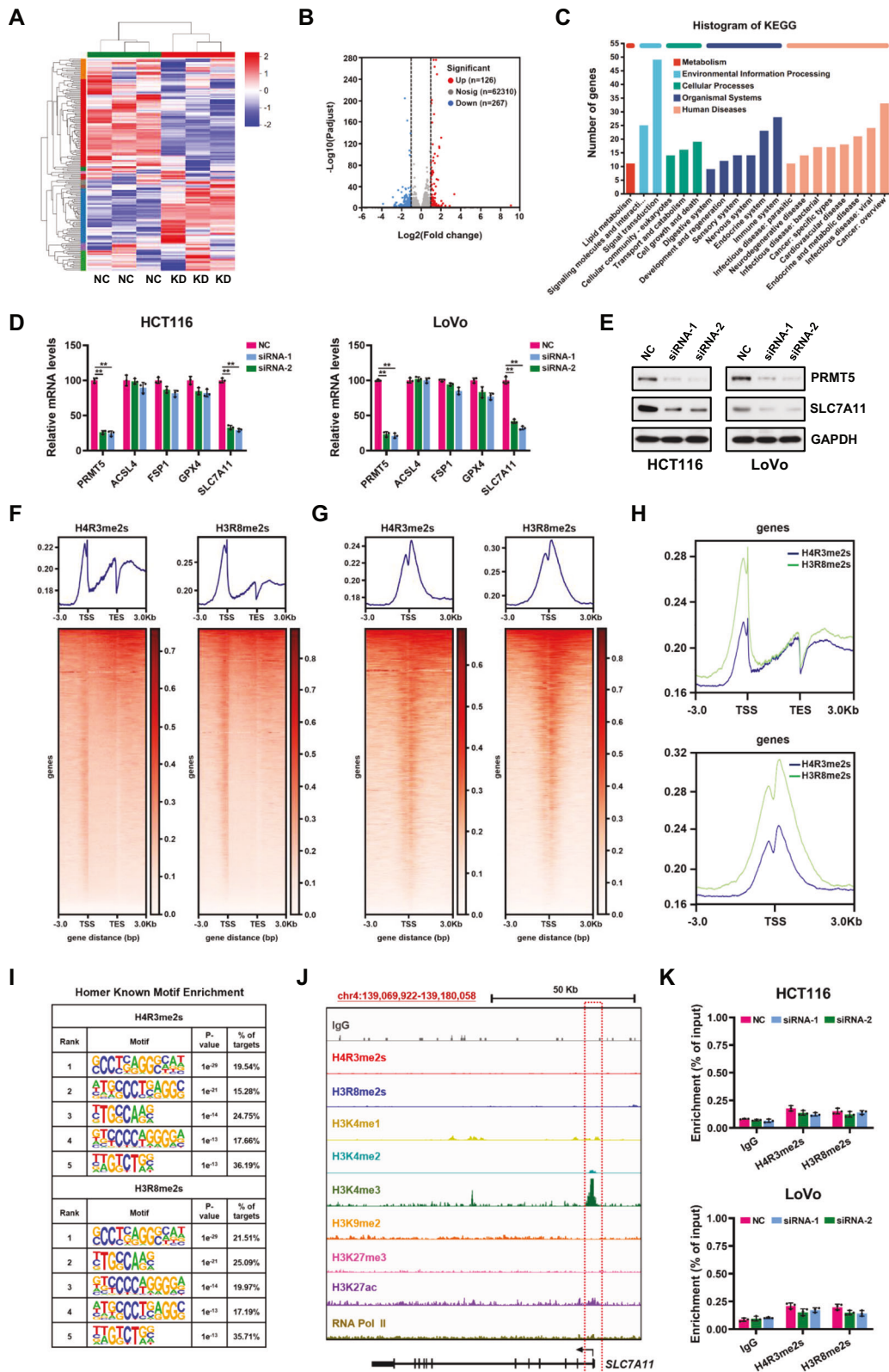
To further verify the role of PRMT5 in ferroptosis in vivo, a mouse xenograft model was established by using stable NC and PRMT5-depleted (sh_PRMT5) HCT116 cells, and tumors were treated with Erastin or Fer-1. As can be seen in Fig. 2I, J, the tumor growth curve of sh_PRMT5 group grew more slowly than that in the control group, whereas Fer-1 treatment significantly increased the growth rate of these xenografts. The xenografts formed by sh_PRMT5 cells were smaller and lighter, and these effects were reversed by Fer-1 (Fig. 2K); the same results were observed with IHC staining for Ki-67 (Fig. 2L). Moreover, xenografts formed by sh_PRMT5 cells showed higher MDA and lipid ROS levels than those formed by control cells; however, these effects were partially reversed by Fer-1 (Fig. 2M, N). Collectively, these findings demonstrated that PRMT5 exerts ferroptosis-suppressive effects in CRC.

PRMT5 facilitates the expression of SLC7A11 in CRC cells

To explore the molecular mechanisms underlying the ferroptosis-suppressive roles of PRMT5, we conducted RNA-seq analysis using high throughput Illumina sequencing to characterize the transcriptomic alterations in PRMT5-depleted HCT116 cells (Fig. 3A). Compared with the control, a total of 393 differentially expressed genes (DEGs) were identified (FDR value ≤ 0.001 and $|\log_2(\text{Fold change})| \geq 1$), including 126 upregulated and 267 downregulated genes (Fig. 3B). KEGG analysis revealed that DEGs were significantly enriched in several key cellular processes, such as lipid metabolism, signal transduction, transport and catabolism, cell growth and death (Fig. 3C). Among these DEGs, we focused on SLC7A11, which has been well-established as a critical ferroptosis regulator. Through qRT-PCR analysis, we found that SLC7A11 was significantly downregulated in PRMT5-depleted HCT116 and LoVo cells, whereas other ferroptosis-related genes, such as ACSL4, FSP1 and GPX4, were not markedly affected (Fig. 3D). Moreover, Western blotting analysis showed that siRNA-mediated knockdown of PRMT5 obviously reduced the protein levels of SLC7A11 in HCT116 and LoVo cells (Fig. 3E).

To probe whether PRMT5 directly regulates SLC7A11 transcription, we performed CUT&Tag analysis using anti-H4R3me2s and anti-H3R8me2s antibodies in HCT116 cells. Genome-wide CUT&Tag analysis uncovered the genome-wide binding profile of PRMT5-dependent H4R3me2s and H3R8me2s. Notably, we observed that H4R3me2s and H3R8me2s were mainly enriched around the transcription start sites (TSS) of genes, indicating that these two marks are tightly linked to transcriptional modulation (Fig. 3F, G). Interestingly, these two histone modifications exhibited exceedingly similar genome-wide binding patterns (Fig. 3H and Fig. S3A), as well as known enriched DNA binding sites by HOMER known motif analysis (Fig. 3I). KEGG analysis revealed that these two histone marks were associated with multiple biological processes, including cAMP, PI3K-Akt, Wnt, Rap1 signaling pathways (Fig. S3B).

Previous studies reported that SLC7A11 was transcriptionally activated in CRC cells. According to ChIP-seq datasets publicly available at NCBI GEO database, we found that active histone marks, such as H3K4me1, H3K4me2, H3K4me3 and H3K27ac, and RNA polymerase II (RNA Pol II) were located around the TSS of SLC7A11 gene in HCT116 cells, whereas repressive histone marks were not, such as H3K9me2 and H3K27me3 (Fig. 3J), implicating that SLC7A11 was activated at the transcriptional level in CRC cells. Surprisingly, CUT&Tag analysis revealed that there were no clear H4R3me2s and H3R8me2s peaks around the TSS of SLC7A11 gene, suggesting that PRMT5 is not a direct transcription modulator of SLC7A11. To further validate whether PRMT5-mediated H4R3me2s and H3R8me2s marks participate in the regulation of SLC7A11, ChIP-qPCR assays were performed using H4R3me2s and H3R8me2s antibodies in HCT116 and LoVo cells. Indeed, ChIP-qPCR results confirmed that PRMT5-mediated H4R3me2s and H3R8me2s were not significantly enriched around the TSS of SLC7A11 gene in HCT116 and LoVo cells (Fig. 3K). Taken together, PRMT5 facilitates the expression of SLC7A11 in CRC cells, but not at the transcription level.



Data derived from GEPIA database confirmed that the expression of SLC7A11 was upregulated in most of human cancers, including COAD (Fig. S3C, D). Moreover, survival analysis of SLC7A11 in CRC was conducted with the online Kaplan-Meier Plotter database. As shown in Fig. S3E, high expression of

SLC7A11 statistically correlated with shorter overall survival of CRC patients.

To uncover whether PRMT5 knockdown exerts ferroptosis-promoting role through downregulating the expression of SLC7A11, we restored the expression of SLC7A11 through

Fig. 3 PRMT5 facilitates the expression of SLC7A11 in CRC cells. **A** Hierarchical clustering map shows the significantly differentially expressed genes in NC or PRMT5 siRNAs-transfected (KD) HCT116 cells by RNA-seq. **B** Volcano plot of differentially expressed genes. The red ($n = 126$) and blue ($n = 267$) dots represent upregulated and downregulated genes, respectively. **C** KEGG enrichment analysis of differentially expressed genes. **D** The relative expression levels of mRNAs were detected by qRT-PCR in NC or PRMT5 siRNAs-transfected HCT116 and LoVo cells. **E** The protein levels of SLC7A11 were examined by Western blotting in NC or PRMT5 siRNAs-transfected HCT116 and LoVo cells. **F–H** Heatmaps and metagene plots show the genome-wide enrichment of H4R3me2s and H3R8me2s signals around the TSS or gene body in HCT116 cells by CUT&Tag analysis. **I** HOMER was used to identify known motifs of H4R3me2s and H3R8me2s-binding sites. **J** Representative CUT&Tag tracks for H4R3me2s, H3R8me2s, H3K4me1, H3K4me2, H3K4me3, H3K9me2, H3K27me3, H3K27ac and RNA Pol II at the TSS of SLC7A11 gene. **K** ChIP-qPCR assays were performed to evaluate the deposition of H4R3me2s and H3R8me2s at the TSS of SLC7A11 gene in HCT116 and LoVo cells. The data shown represent the mean \pm SD. $^{**}P < 0.01$.

transfecting the recombinant eukaryotic expression vector pcDNA3.1-SLC7A11 into PRMT5-depleted HCT116 and LoVo cells. The re-expression of SLC7A11 at the mRNA and protein levels in PRMT5-depleted HCT116 and LoVo cells was verified by qRT-PCR and Western blotting (Fig. S4A, B). Re-expression of SLC7A11 significantly reversed the ferroptotic death of PRMT5-deficient HCT116 and LoVo cells induced by Erastin or RSL3 (Fig. S4C, D). Compared to sh_PRMT5 cells (Fig. S4E–I), MDA, lipid ROS and Fe^{2+} levels were significantly decreased in HCT116 and LoVo cells with combined treatment (sh_PRMT5 + SLC7A11 OE).

Mouse xenograft model was established by subcutaneously injecting stable NC, sh_PRMT5 or sh_PRMT5 + SLC7A11 OE HCT116 cells into nude mice, and tumors were treated with Erastin. As can be seen in Fig. S4J, K, the tumor growth curve of sh_PRMT5 group grew more slowly than that in the control group (NC), whereas SLC7A11 restoration significantly increased the growth rate of these xenografts. The xenografts formed by sh_PRMT5 cells were smaller and lighter, and these effects were reversed by the re-expression of SLC7A11 (Fig. S4L). The IHC images showed that SLC7A11 restoration accelerated the growth of sh_PRMT5 xenografts, as evidenced by increased Ki-67 expression (Fig. S4M). Furthermore, xenografts formed by sh_PRMT5 + SLC7A11 OE HCT116 cells showed lower MDA and lipid ROS levels than those formed by sh_PRMT5 cells (Fig. S4N, O). Collectively, we concluded that PRMT5 inhibits ferroptosis of CRC cells through upregulating the expression of SLC7A11.

PRMT5 upregulates the expression of SLC7A11 through transcriptionally inhibiting the expression of ALKBH5

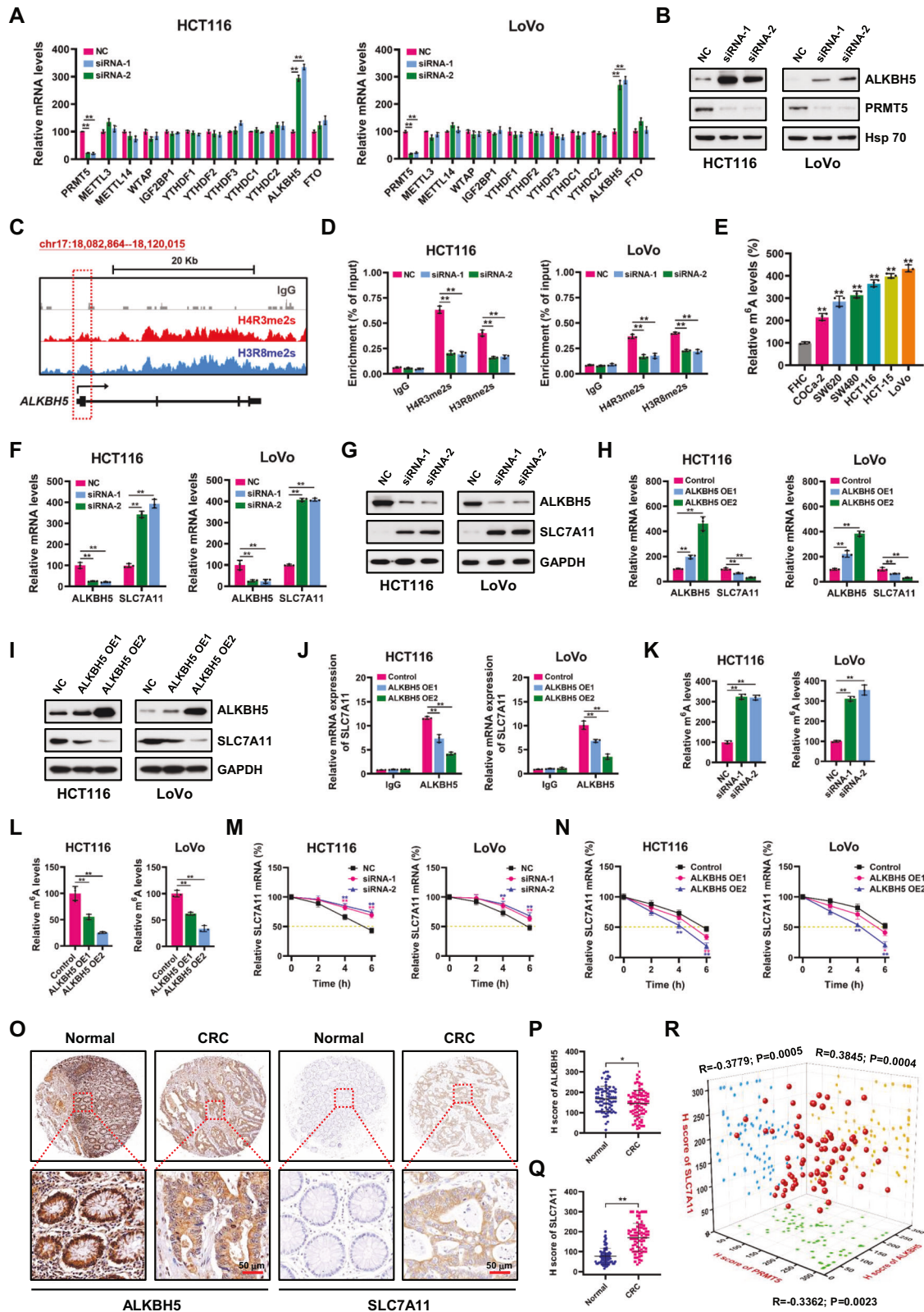
Given that PRMT5-mediated SLC7A11 activation in CRC cells is not at the transcription level, we speculate with the possibility that PRMT5 may contribute to the mRNA stability of SLC7A11. N^6 -methyladenosine (m^6A) is the most predominant mRNA modification in eukaryotes, which modulates mRNA stability, thereby fine-tuning gene regulation at the post-transcriptional level [34]. To examine whether PRMT5 participates in regulating potential m^6A -related genes, qRT-PCR was performed to determine the expression levels of known m^6A “writers” (METTL3, METTL14 and WTAP), “readers” (IGF2BP1, YTHDF1, YTHDF2, YTHDF3, YTHDC1 and YTHDC2) and “erasers” (ALKBH5 and FTO) in PRMT5-deficient HCT116 and LoVo cells. Interestingly, qRT-PCR results revealed that ALKBH5 was significantly higher in PRMT5-depleted HCT116 and LoVo cells than that in control cells (Fig. 4A). Upregulation of ALKBH5 was further validated at the protein level in PRMT5-silenced HCT116 and LoVo cells by Western blotting (Fig. 4B). CUT&Tag analysis showed that PRMT5-mediated H4R3me2s and H3R8me2s directly bound to ALKBH5 gene in HCT116 cells (Fig. 4C). ChIP-qPCR assays demonstrated that both H4R3me2s and H3R8me2s marks were significantly enriched around the TSS of ALKBH5 gene in HCT116 and LoVo cells (Fig. 4D). The occupancies of H4R3me2s and H3R8me2s were dramatically reduced in HCT116 and LoVo cells upon PRMT5 knockdown. These findings elicited that ALKBH5 is a transcriptional target of PRMT5 in CRC cells.

ALKBH5 is a well-described m^6A “eraser” that impacts the fate of mRNA in a m^6A -dependent manner [35]. To explore the potential

m^6A modification in CRC, we determined m^6A modification levels in six CRC cell lines (CoCa-2, SW620, SW480, HCT116, HCT-15 and LoVo) and colonic mucosal epithelial cell line (FHC) by m^6A RNA methylation quantification assay kit. The relative m^6A modification levels were upregulated in CRC cells relative to the FHC cell line (Fig. 4E). To determine whether ALKBH5 modulates the expression of SLC7A11, qRT-PCR and Western blotting were performed in HCT116 and LoVo cells. Compared to those in control cells, the mRNA and protein levels of SLC7A11 were dramatically increased in ALKBH5-deficient HCT116 and LoVo cells (Fig. 4F, G), whereas it was downregulated when ALKBH5 was overexpressed (Fig. 4H, I), suggesting that ALKBH5 negatively regulates the expression of SLC7A11. Since ALKBH5 is a key “eraser” in the m^6A modification process, we propose that ALKBH5 regulates the expression of SLC7A11 in the m^6A -dependent manner. Through RIP-qPCR assay, we found that SLC7A11 mRNA was precipitated by anti-ALKBH5 antibody, and ALKBH5 overexpression could significantly decrease the SLC7A11 mRNA enrichment (Fig. 4J). Moreover, the relative m^6A modification levels in HCT116 and LoVo cells were dramatically increased in ALKBH5-deficient HCT116 and LoVo cells, whereas it was downregulated when ALKBH5 was overexpressed (Fig. 4K, L). RNA stability assays revealed that ALKBH5 knockdown significantly enhanced the mRNA stability of SLC7A11 in HCT116 and LoVo cells, whereas ALKBH5 overexpression remarkably reduced the mRNA stability of SLC7A11 (Fig. 4M, N).

The expression levels of ALKBH5 and SLC7A11 in CRC tissues ($n = 80$) were detected by IHC staining. Immunoreactive signal of ALKBH5 was distributed in both the nucleus and cytoplasm of tumor cells, whereas SLC7A11 was preferentially expressed in the membrane of tumor cells (Fig. 4O). H score analysis revealed that the expression of ALKBH5 in CRC tissues was significantly lower than that in the matched adjacent normal tissues (Fig. 4P). On the contrary, SLC7A11 was found to be remarkably upregulated in CRC tissues (Fig. 4Q). Spearman correlation analysis, as shown in Fig. 4R, revealed that H score of PRMT5 was positively correlated with SLC7A11 in CRC samples ($R = 0.3845$; $P = 0.0004$). H score of ALKBH5 was negatively correlated with H scores of PRMT5 ($R = -0.3362$; $P = 0.0023$) and SLC7A11 ($R = -0.3779$; $P = 0.0005$).

Encouraged by the above results, we want to know whether ALKBH5 modulates ferroptosis of CRC cells through inhibiting the expression of SLC7A11. We recovered the expression of SLC7A11 in ALKBH5-overexpressed HCT116 and LoVo cells, verified by qRT-PCR and Western blotting (Fig. S5A, B). We observed that overexpression of SLC7A11 (ALKBH5 OE + SLC7A11 OE) dramatically attenuated the Erastin or RSL3-induced ferroptotic death of ALKBH5-overexpressed HCT116 and LoVo cells (Fig. S5C–E). Compared to control cells, ALKBH5 overexpression (Fig. S5F–J) significantly increased the contents of MDA, lipid ROS and Fe^{2+} in HCT116 and LoVo cells, suggesting that ALKBH5 overexpression promotes the ferroptosis of CRC cells. However, restoration of SLC7A11 expression (ALKBH5 OE + SLC7A11 OE) effectively reversed the promotive role of ALKBH5 overexpression (ALKBH5 OE) in ferroptosis, as evidenced by the decreased levels of MDA, lipid ROS and Fe^{2+} levels. Thus, these data demonstrate that ALKBH5 overexpression accelerates ferroptosis of CRC cells through inhibiting the expression of SLC7A11.



PRMT5 is lactylated at K240 in CRC

Lactylation is a novel lactate-derived posttranslational modification that plays important roles in multiple cellular processes [36]. First, to confirm whether lactylation is involved in the progression of CRC, we examined the pan lysine lactylation (pan-Kla) level in

CRC tissues by IHC staining. As shown in Fig. S6A, B, pan-Kla level was significantly upregulated in the CRC tissues compared with the normal tissues. To characterize the landscape of lactylation in CRC, we collected 10 pairs of CRC and adjacent normal tissues, and then applied lacticome analysis by the 4D label-free

Fig. 4 PRMT5 upregulates the expression of SLC7A11 through transcriptionally inhibiting the expression of ALKBH5. **A** The relative expression levels of mRNAs were detected by qRT-PCR in NC or ALKBH5 siRNAs-transfected HCT116 and LoVo cells. **B** The protein level of ALKBH5 was verified by Western blotting in NC or PRMT5 siRNAs-transfected HCT116 and LoVo cells. **C** Representative CUT&Tag tracks for H4R3me2s and H3R8me2s at the ALKBH5 gene in HCT116 cells. **D** ChIP-qPCR assays were performed to evaluate the depositions of H4R3me2s and H3R8me2s at the TSS of ALKBH5 gene in HCT116 and LoVo cells. **E** The total m⁶A modification levels in CRC cells were determined by m⁶A RNA methylation quantification assay kit. **F, G** The relative expression levels of SLC7A11 mRNA and protein were detected in NC and ALKBH5 siRNAs-transfected HCT116 and LoVo cells by qRT-PCR and Western blotting, respectively. **H, I** The relative expression levels of SLC7A11 mRNA and protein were examined in vector, ALKBH5 OE1 (1 µg) or ALKBH5 OE2 (2 µg)-transfected HCT116 and LoVo cells by qRT-PCR and Western blotting, respectively. **J** RIP assay demonstrated the SLC7A11 mRNA enrichment precipitated by anti-IgG or anti-ALKBH5 antibodies in vector, ALKBH5 OE1 (1 µg) or ALKBH5 OE2 (2 µg)-transfected HCT116 and LoVo cells. **K** The total m⁶A modification levels were determined in NC or ALKBH5 siRNAs-transfected HCT116 and LoVo cells. **L** The total m⁶A modification levels were determined in vector, ALKBH5 OE1 (1 µg) or ALKBH5 OE2 (2 µg)-transfected HCT116 and LoVo cells. **M, N** Stability of SLC7A11 mRNA was assessed by qRT-PCR in ALKBH5 depleted or overexpressed HCT116 and LoVo cells after treatment with Actinomycin D. **O–Q** IHC staining and H scores for ALKBH5 and SLC7A11 in CRC (n = 80) and matched adjacent normal tissues (n = 80). Scale bar, 50 µm. **R** Scatter plot of PRMT5, ALKBH5 and SLC7A11 levels in CRC tissues (n = 80). All P values and R values were calculated with Spearman's r test. The data shown represent the mean ± SD. *P < 0.05, **P < 0.01.

quantification mass spectrometry to screen differentially lactylated proteins in CRC samples. For the details of the lactylome data, a total of 179 sites of 119 proteins with increased lactylation and 7 sites of 6 proteins with decreased lactylation (Fig. 5A, B). The most of these differentially lactylated proteins were distributed in the nucleus (44.72%) and cytoplasm (39.02%) of CRC cells (Fig. 5C). GO enrichment analysis revealed that differentially lactylated proteins were mainly involved in regulation of protein metabolic process, programmed cell death and apoptotic process, etc. (Fig. 5D). KEGG analysis showed that differentially lactylated proteins were mainly involved in cell growth and death, cellular community, cell motility, transport and catabolism, etc. (Fig. 5E).

Notably, mass spectrometry analysis uncovered that PRMT5 is lactylated at lysine 240 (PRMT5 K240lac; Fig. 5F). The lysine residue at position 240 (K240) is located in the triosephosphate isomerase barrel (TIM-barrel) domain of PRMT5, which is highly conserved among different species (Fig. 5G). To further confirm PRMT5 K240 lactylation, a PRMT5 K240lac antibody was produced and affinity-purified in Jingjie PTM Biolabs. By using the antibody, we carried out Co-IP experiments using anti-pan-Kla or anti-PRMT5 K240lac antibodies to precipitate PRMT5 in HCT116 and LoVo cells. Associated proteins from cellular extracts of HCT116 and LoVo cells were detected by Western blotting. As shown in Fig. 5H, I, we observed that endogenous PRMT5 was successfully co-precipitated with anti-pan-Kla or anti-PRMT5 K240lac antibodies, suggesting that PRMT5 was lactylated in CRC cells.

K240lac is essential for PRMT5 to modulate ALKBH5/SLC7A11 axis

To investigate the functional significance of K240 lactylation in PRMT5, we employed a site-directed mutagenesis strategy by substituting lysine 240 with arginine (K240R) - a charge-conservative mutation that preserves the cationic properties of this residue. This approach specifically eliminates the post-translational lactylation while maintaining the structural integrity of PRMT5 protein. Cells with PRMT5 K240R mutation were obtained by transfecting PRMT5-depleted HCT116 and LoVo cells with lentivirus containing cDNA of the PRMT5 K240R mutant. Through qRT-PCR and Western blotting assays (Fig. 6A, B), we observed that PRMT5 WT overexpression increased the level of PRMT5 K240lac, accompanied with the downregulation of ALKBH5 and upregulation of SLC7A11. However, this effect was almost eliminated when PRMT5 K240R mutant was overexpressed in PRMT5-depleted HCT116 and LoVo cells. Following these findings, we investigated whether PRMT5 K240R mutation influences the depositions of H4R3me2s and H3R8me2s at the TSS of ALKBH5 gene by ChIP-qPCR experiment. Intriguingly, as shown in Fig. 6C, we observed striking loss of H4R3me2s and H3R8me2s enrichment at the TSS of ALKBH5 gene in PRMT5 K240R-overexpressed HCT116 and LoVo cells. Since PRMT5 K240R upregulates the expression of ALKBH5, we propose that PRMT5 K240lac affects

ALKBH5-mediated m⁶A modification. We performed RIP-qPCR assays when PRMT5 WT or K240R mutant was overexpressed in PRMT5-depleted HCT116 and LoVo cells. As shown in Fig. S7A, we found that SLC7A11 mRNA was precipitated by anti-ALKBH5 antibody, and PRMT5 K240R significantly decreased the SLC7A11 mRNA enrichment, indicating that PRMT5 K240lac affects ALKBH5-mediated m⁶A modification.

IHC staining showed that high expression levels of PRMT5, PRMT5 K240lac, H4R3me2s and H3R8me2s were detected in CRC cases (Fig. 6D, E and Fig. S7B, C). Correlation analysis based on IHC staining revealed that the level of PRMT5 was positively correlated with PRMT5 K240lac ($R = 0.5904$; $P < 0.0001$), H4R3me2s ($R = 0.6041$; $P < 0.0001$) and H3R8me2s ($R = 0.7408$; $P < 0.0001$) levels in CRC tissues (Fig. 6F). Moreover, upregulated expression of PRMT5 K240lac was significantly associated with higher histological tumor grade of patients with CRC; however, it was not correlated with age, gender, tumor stage, lymph node and distant metastasis. (Table S1). Further correlation analysis uncovered that the expression of PRMT5 K240lac was positively correlated with H4R3me2s ($R = 0.6979$; $P < 0.0001$), H3R8me2s ($R = 0.4751$; $P < 0.0001$) and SLC7A11 ($R = 0.5685$; $P < 0.0001$) levels, and was negatively correlated with ALKBH5 ($R = -0.3433$; $P = 0.0018$) in CRC samples (Fig. 6G, H). Furthermore, as shown in Fig. S7D, Kaplan-Meier survival analysis revealed that CRC patients with high PRMT5 K240lac expression suffered from worse survival outcomes than patients with a low PRMT5 K240lac expression (Log-rank; $P < 0.001$).

PRMT5 K240R sensitizes CRC cells to ferroptosis

The above findings prompted us to investigate whether PRMT5 K240lac can in fact drive CRC progression through modulating the ferroptosis of CRC cells. PRMT5 WT or K240R mutant were introduced into PRMT5-depleted HCT116 and LoVo cells. To overexpress PRMT5 WT or K240R mutant in PRMT5-depleted HCT116 and LoVo cells, shRNA-resistant PRMT5 WT or K240R constructs were stably expressed in HCT116 and LoVo cells referring to our previous study [37]. By using the CCK-8 assay kit, the results demonstrated that PRMT5 WT overexpression inhibited the Erastin- and RSL3-triggered ferroptosis of HCT116 and LoVo cells compared with the vector control group (Fig. 7A–D and Fig. S8A, B), whereas the inhibition effect of PRMT5 on ferroptosis was diminished when PRMT5 K240R was re-expressed. To further investigate the impact of PRMT5 K240R on ferroptosis in CRC cells, we determined the contents of MDA, lipid ROS and Fe²⁺ in PRMT5 WT or K240R-overexpressed HCT116 and LoVo cells. Compared to PRMT5 WT cells (Fig. 7E–I), PRMT5 K240R significantly increased the contents of MDA, lipid ROS and Fe²⁺, suggesting that PRMT5 K240R overexpression promotes Erastin- and RSL3-induced ferroptosis of HCT116 and LoVo cells.

PRMT5 WT or K240R HCT116 cells xenografted in nude mouse model was used to verify the role of PRMT5 K240lac in vivo. As can

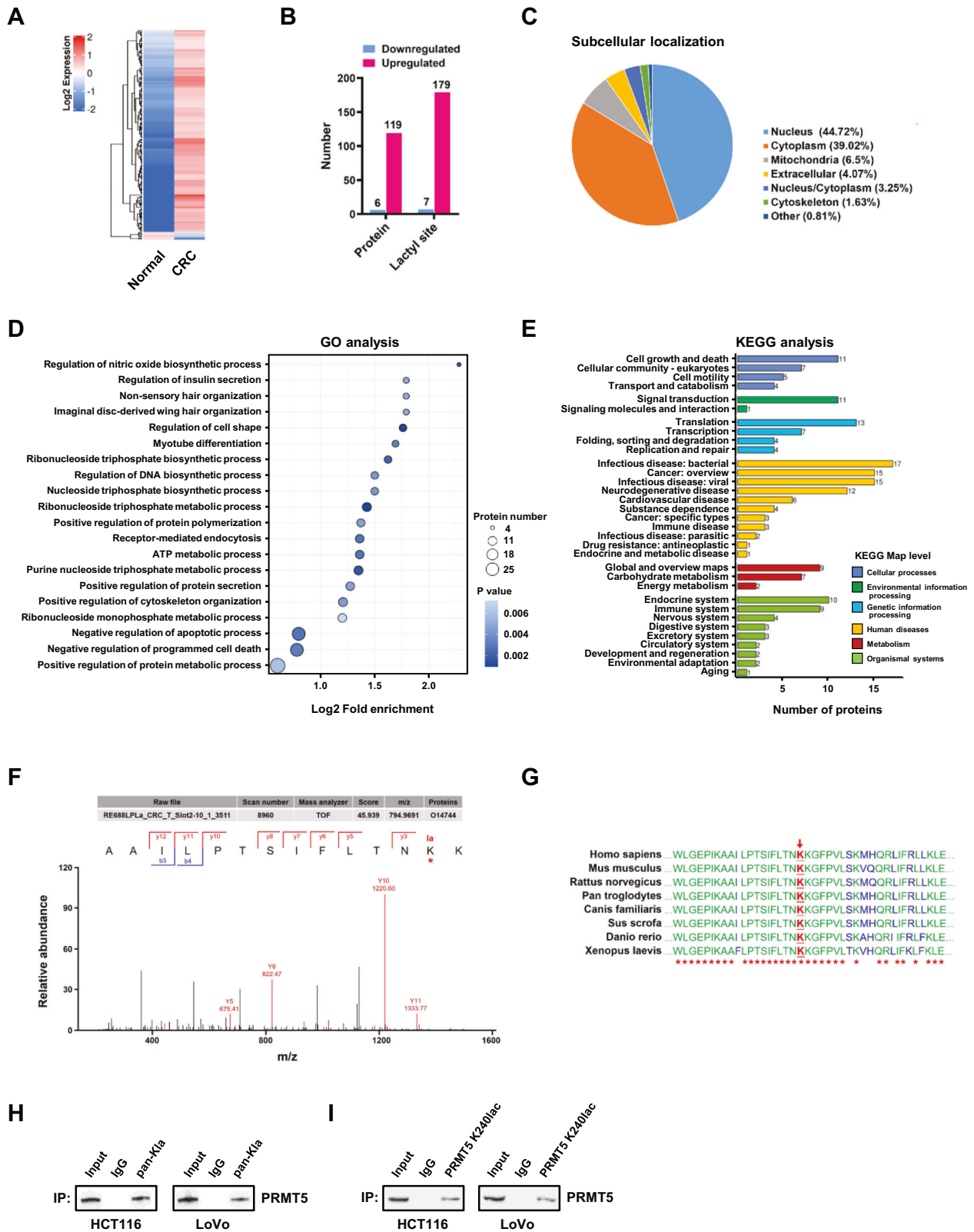
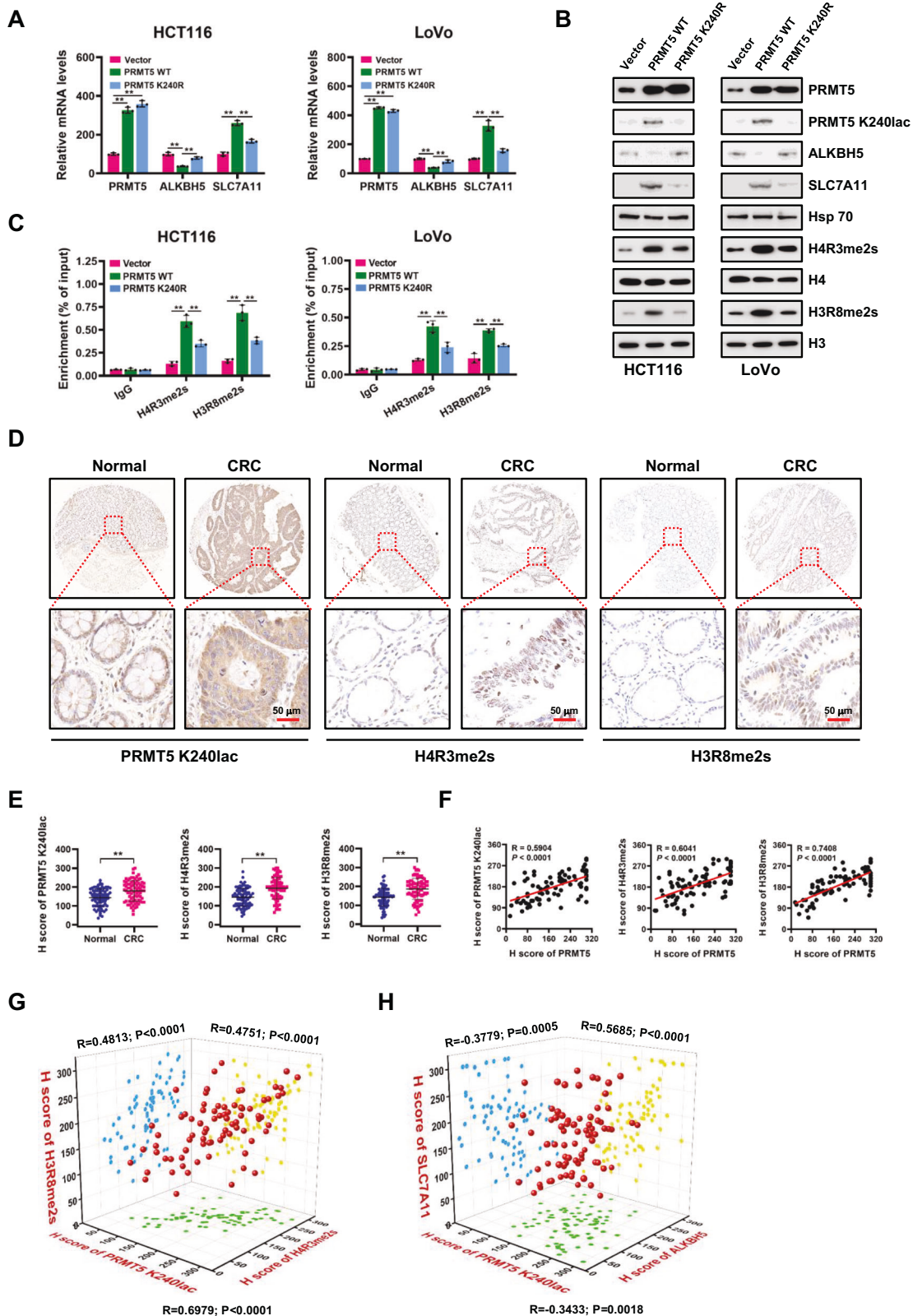


Fig. 5 PRMT5 is lactylated at K240 in CRC. **A** Heatmap shows the differentially expressed lactylated proteins in CRC ($n = 10$) and adjacent normal ($n = 10$) tissues. **B** Differentially expressed lactylated proteins (119 upregulated and 6 downregulated) and sites (179 upregulated and 7 downregulated) were identified in CRC tissues. **C** The pie chart indicates the subcellular localization of differentially expressed lactylated proteins in CRC. **D, E** GO and KEGG enrichment analysis revealed the biological functions of differentially expressed lactylated proteins. **F** Mass spectra for PRMT5 peptides lactylated at K240. **G** K240 of PRMT5 is highly conserved among different species. **H, I** Co-IP experiments were performed using anti-pan-Kla or anti-PRMT5 K240lac antibodies to precipitate PRMT5 in HCT116 and LoVo cells.



be seen in Fig. 7J, K, the tumor growth curve of PRMT5 K240R group grew more slowly than that in the control group, whereas Fer-1 treatment significantly promoted the growth of these tumors. The xenografts formed by PRMT5 K240R HCT116 cells were much smaller than that of control group, accompanied by

increased ALKBH5 and decreased PRMT5 K240lac, SLC7A11, Ki-67 levels (Fig. S8C). Moreover, PRMT5 K240R resulted in higher MDA levels than those formed by control cells (Fig. 7L). In conclusion, we demonstrated that PRMT5 K240R sensitizes CRC cells to ferroptosis in vitro and in vivo.

Fig. 6 K240Iac is essential for PRMT5 to modulate ALKBH5/SLC7A11 axis. **A** The relative mRNA expression levels of PRMT5, ALKBH5 and SLC7A11 were determined by qRT-PCR in vector, PRMT5 WT- and PRMT5 K240R-overexpressed HCT116 and LoVo cells. **B** Protein levels of PRMT5, PRMT5 K240Iac, ALKBH5, SLC7A11, H4R3me2s and H3R8me2s were detected in vector, PRMT5 WT- and PRMT5 K240R-overexpressed HCT116 and LoVo cells by Western blotting. **C** ChIP-qPCR assays were performed to evaluate the depositions of H4R3me2s and H3R8me2s at the TSS of ALKBH5 gene in vector, PRMT5 WT- and PRMT5 K240R-overexpressed HCT116 and LoVo cells. **D** IHC staining for PRMT5 K240Iac, H4R3me2s and H3R8me2s in CRC and adjacent normal tissues. Scale bars, 50 μ m. **E** H scores of PRMT5 K240Iac, H4R3me2s and H3R8me2s in CRC (n = 80) and matched adjacent normal tissues (n = 80). **F** Spearman correlation analysis of PRMT5 and PRMT5 K240Iac, PRMT5 and H4R3me2s, and PRMT5 and H3R8me2s in CRC (n = 80) and matched adjacent normal tissues (n = 80). **G** Scatter plot of PRMT5 K240Iac, H4R3me2s and H3R8me2s levels in CRC tissues (n = 80). **H** Scatter plot of PRMT5 K240Iac, ALKBH5 and SLC7A11 levels in CRC tissues (n = 80). All P values and R values were calculated with Spearman's r test. The data shown represent the mean \pm SD. **P < 0.01.

DISCUSSION

Emerging evidence highlights the potential roles of PRMT5 in modulating ferroptosis across different cancer types, especially in triple-negative breast cancer (TNBC). For example, PRMT5 drives ferroptosis resistance by selectively methylating KEAP1, a negative regulator of the antioxidant transcription factor NRF2. This methylation stabilizes KEAP1, leading to NRF2 degradation and subsequent suppression of the NRF2/HMOX1 axis, which reduces intracellular iron accumulation and lipid peroxidation [38]. Furthermore, PRMT5 catalyzes the symmetric dimethylation of GPX4 at arginine 152 (R152), preventing its ubiquitination and degradation by the Cullin1-FBW7 E3 ligase complex, thereby enhancing GPX4 stability and conferring resistance to ferroptosis inducers [39]. However, the role of PRMT5 in the ferroptosis of CRC cells remains less defined. In the present study, we identified the PRMT5/ALKBH5/SLC7A11 axis as part of an important mechanism underlying ferroptosis resistance. As illustrated in Fig. 7M, lactylated PRMT5 repressed the expression of ALKBH5 via H4R3me2s and H3R8me2s at the transcription level, which enhances the stability of SLC7A11 mRNA and upregulates its expression in an m⁶A-dependent manner, thus aggravating CRC progression through attenuating ferroptosis.

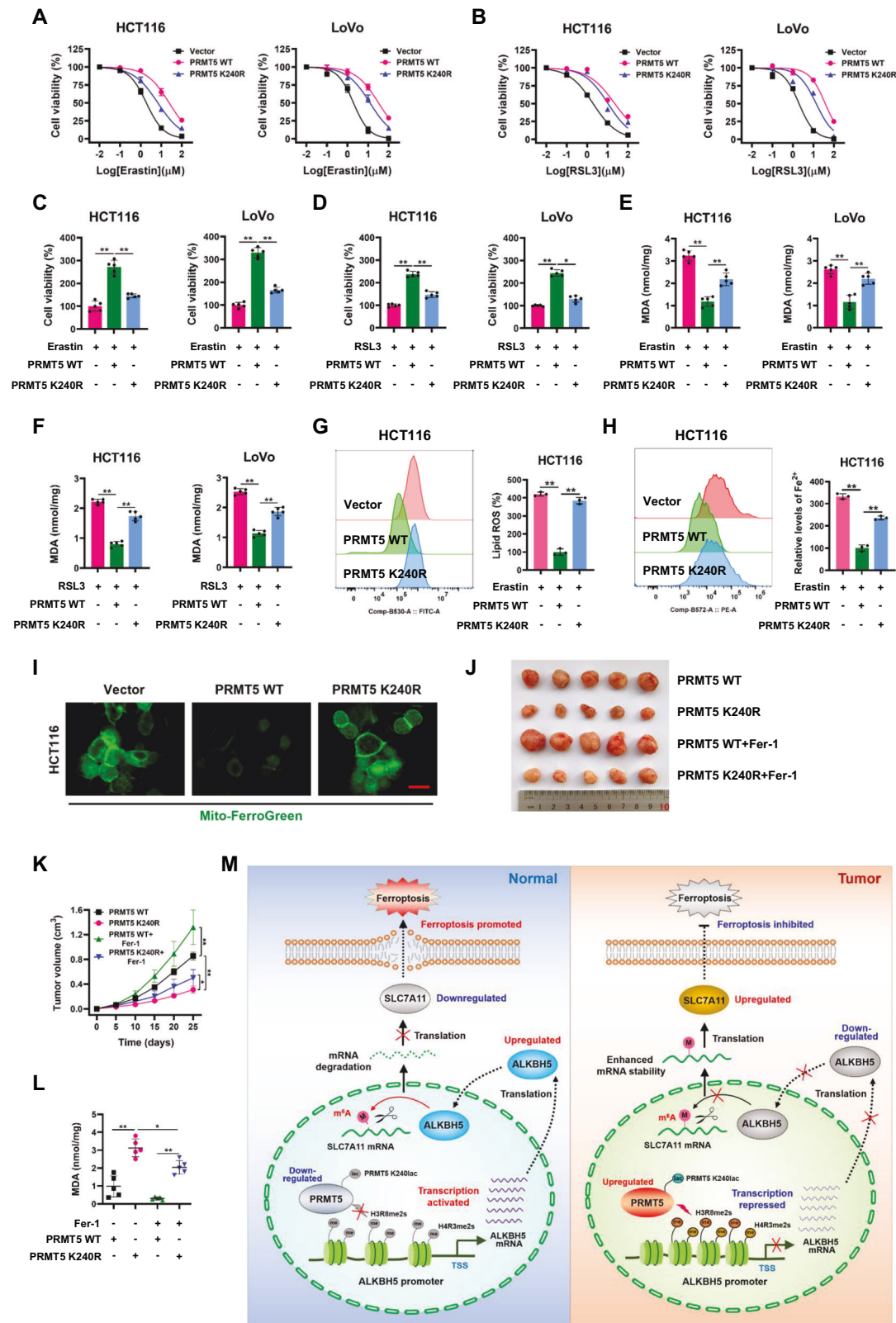
Epigenetic modifier PRMT5 is the major type II arginine methyltransferase that catalyzes the formation of symmetric dimethylarginine residues in a number of nuclear and cytoplasmic proteins [26]. The resultant symmetrically dimethylated arginine on histone H3 or H4 (H3R8me2s and H4R3me2s) are critical epigenetic modifications mediated by PRMT5 that are usually associated with gene silencing. In this study, CUT&Tag in combination with ChIP analyses revealed that PRMT5-dependent H4R3me2s and H3R8me2s signals located in the vicinity of TSS of ALKBH5 gene, thus resulting in transcriptional inactivation of ALKBH5. CUT&Tag profiling using anti-PRMT5 antibodies is an unbiased genome-wide approach to map the PRMT5 deposition in CRC cells, as well as its histone substrates (H4R3me2s and H3R8me2s). Unfortunately, our CUT&Tag experiments using commercially available anti-PRMT5 antibodies were unsuccessful despite that we repeated the experiment many times. A possible explanation for this phenomenon is that PRMT5 is extremely dynamic in the nucleus of CRC cells, which transiently interacts with chromatin, and therefore might escape detection.

It is intriguing that PRMT5 inhibits doxorubicin-induced RNA m⁶A methylation by enhancing the nuclear translocation of ALKBH5 with the partner ALKBH7, underscoring the therapeutic potential of targeting the PRMT5-ALKBH5 axis to overcome chemoresistance [40]. A recent study reveals that PRMT5 directly catalyzes the symmetric dimethylation of ALKBH5 at the R316 residue, which triggers TRIM28-mediated ALKBH5 ubiquitination degradation, thus promoting CRC immune evasion via increasing CD276 expression [41]. Taken together, all these lines of evidence indicate that PRMT5 regulates ALKBH5 expression and functions through diverse mechanisms, including post-translational stabilization, spatial regulation (nuclear trafficking), and potential transcriptional or co-regulatory interactions, highlighting the synergistic roles of PRMT5/ALKBH5 in cancer progression and therapy resistance.

As a prominent m⁶A demethylase, ALKBH5 has been recognized to affect the mRNA stability and determine the fate of mRNA in an m⁶A-dependent manner. In such a manner, dysregulation of ALKBH5 coordinates a variety of cellular processes and exerts important regulatory roles in multiple malignancies, mostly via post-transcriptional regulation of oncogenes or tumor suppressors [42]. In CRC, ALKBH5 is tightly associated with tumorigenesis and development, but its role and regulatory mechanism remain controversial. For instance, Zhai et al. showed that high expression of ALKBH5 predicts poor prognosis in patients with CRC. ALKBH5-induced DKK1 recruits immune-suppressive myeloid-derived suppressor cells and inhibits infiltration of antitumor CD8⁺ T and natural killer cells, thereby driving tumorigenesis [43]. Shen et al. reported that ALKBH5 was significantly elevated in CRC samples and could increase the proliferative, migrative and invasive capabilities of CRC cells, indicating that ALKBH5 may be an attractive therapeutic target [44].

In contrast, Luo et al. revealed a tumor suppressive role of ALKBH5 in CRC. They found that ALKBH5 was downregulated in CRC, and restoration of ALKBH5 reduced the mRNA stability of SLC7A11 by erasing m⁶A modification, thus triggering the ferroptosis of CRC cells [45]. Huang et al. reported that ALKBH5 can downregulate SLC7A11 transcription by decreasing m⁶A modification, thus promoting the ferroptosis of non-small cell lung cancer (NSCLC) cells and suppressing NSCLC progression [46]. Moreover, Yang et al. demonstrated that overexpressed ALKBH5 significantly inhibited the invasion and metastasis of CRC cells in vitro and in vivo, suggesting that ALKBH5 acts as a tumor suppressor and may be a potential therapeutic target for CRC [47]. In this study, we observed that ALKBH5 was transcriptionally repressed by PRMT5 in CRC cells. ALKBH5 overexpression could induce the ferroptosis of CRC cells through affecting the mRNA stability of SLC7A11 in an m⁶A-dependent manner. Indeed, increasing evidence in the last years indicates that ALKBH5 plays a crucial tumor-suppressive role in CRC [48–50]. Given the fact that ALKBH5 post-transcriptionally modulates various targets that have distinct functions, we therefore speculate that the role of ALKBH5 in cancer is mainly dependent on its functional targets in a specific cancer type or cellular context.

Lactate accumulation during metabolic processes is used as a precursor for lactylation of histone or non-histone proteins and disrupts the balance of gene transcription, which causes diseases including cancer. Previous studies suggest that histone lactylated modification is involved in many physiological and pathological processes. For instance, lactylation of H4 at K12 (H4K12Iac) activated the transcription of glycolytic genes in macroglia, contributing to the pathogenesis of Alzheimer's disease [51]. Lactylation of H3 at K18 (H3K18Iac) can activate the transcription of the m⁶A binding protein YTHDF2, leading to degradation of PER1 and TP53, thus indicating the potential significance of histone lactylation in tumorigenesis [52]. Through illustrating the links between histone lactylation and cancer hallmarks, histone lactylation is proposed as a promising novel epigenetic code driving cells toward a malignant state, and offers the possibility of developing alternative novel therapeutic strategies [53].



Nonetheless, it remains unclear whether lactate can directly covalently modify non-histone proteins and thus exert potential biological effects in tumorigenesis and cancer progression. In recent years, lactylated non-histone proteins are also gradually being discovered. For example, lactylation of methyltransferase

METTL6 at site K229 under copper stress plays important roles in DLAT lipoylation via m^6A -modification on FDX1 mRNA, and ultimately leads to cuproptosis [54]. The expression of fibroblast growth factor FGF2 is regulated by YY1 K183 lactylation. Besides, elevation of YY1 lactylation increases the expression of FGF2 and

Fig. 7 PRMT5 K240R sensitizes CRC cells to ferroptosis. **A, B** Cell viability was measured by CCK-8 assay in vector, PRMT5 WT- and PRMT5 K240R-overexpressed HCT116 and LoVo cells treated with the indicated doses of Erastin and RSL3. **C, D** Cell viability was measured by CCK-8 assay in vector, PRMT5 WT and PRMT5 K240R-overexpressed HCT116 and LoVo cells treated with 2.5 μ M Erastin or 5 μ M RSL3. **E, F** MDA levels were measured in vector, PRMT5 WT- and PRMT5 K240R-overexpressed HCT116 and LoVo cells treated with 2.5 μ M Erastin or 5 μ M RSL3. **G** Lipid ROS and **H** Fe²⁺ levels were analyzed by flow cytometry in vector, PRMT5 WT- and PRMT5 K240R-overexpressed HCT116 cells treated with 2.5 μ M Erastin. **I** Fluorescence staining of ferrous ion was detected with Mito-FerroGreen dye in vector, PRMT5 WT- and PRMT5 K240R-overexpressed HCT116 cells treated with 2.5 μ M Erastin. Scale bars, 25 μ m. **J** Image of subcutaneous xenografts derived from vector, PRMT5 WT and PRMT5 K240R nude mice treated with Erastin or Fer-1. **K** Tumor volumes of different groups were measured. **L** MDA levels of different groups were measured. **M** Schematic diagram illustrates the mechanism of PRMT5 K240lac/ALKBH5/SLC7A11 axis in facilitating ferroptosis resistance of CRC cells. The data shown represent the mean \pm SD. * P < 0.05, ** P < 0.01.

promotes angiogenesis, while YY1 mutation at K183 eliminates these effects [31]. Moreover, homologous recombination (HR) protein MRE11 is lactylated at K673 by the CBP acetyltransferase, which is linked to DNA double stranded break (DSB) repair [55]. Whether there are numerous lactylated modifications on non-histone proteins in CRC and how these lactylated non-histone proteins work are urgently needed to be elucidated.

Through the protein lactylome analysis of human CRC tissues and cell lines, Xie et al. identified that translation initiation factor eEF1A2 is lactylated at K408, leading to boosted translation elongation and enhanced protein synthesis, which contributes to tumorigenesis [56]. Cheng et al. investigated proteome-wide lactylation in FHC and SW480 cells through mass spectrometry. Intriguingly, they further showed that the enzyme activity of phosphofructokinase-platelet (PFKP) was attenuated by the lactylation of PFKP at K688, which facilitates the aerobic glycolysis and consequently promotes the progression of CRC [57]. In this study, we uncovered a novel regulatory mechanism by which the lactylation of PRMT5 at K240 (PRMT5 K240lac) facilitates the expression of SLC7A11. PRMT5 K240lac is necessary for regulating the expression of SLC7A11 and ferroptosis resistance of CRC cells, while mutation at the PRMT5 lactylation site (PRMT5 K240R) eliminated these effects. Although the lactylation of PRMT5 (PRMT5 K240lac) has been demonstrated to be important for ferroptosis resistance, it is still less understood about the details of how the lactylation is regulated in CRC. Recent progress in cancer metabolism research has identified lactate, a byproduct of the Warburg effect, as a primary driver of lactylation [58]. Elevated lactate levels-ranging from 10 to 30 mM, as frequently observed in cancer cells are required for lactylation formation. This implies that any factor influencing glycolysis, particularly the activity of lactate dehydrogenase A (LDHA), may modulate the lactylation level of PRMT5 (PRMT5 K240lac) [59, 60].

In summary, we herein revealed a novel role of the PRMT5 K240lac/ALKBH5/SLC7A11 axis in the regulation of ferroptosis resistance during the progression of CRC. This finding is of paramount significance in deciphering the molecular mechanism involved in ferroptosis resistance of CRC cells, thus providing a potential target in preventing the development of CRC in clinical practice.

DATA AVAILABILITY

The datasets used in the current study are available from the corresponding author on reasonable request.

REFERENCES

- Yang WS, Stockwell BR. Ferroptosis: death by lipid peroxidation. *Trends Cell Biol.* 2016;26:165–76.
- Jiang X, Stockwell BR, Conrad M. Ferroptosis: mechanisms, biology and role in disease. *Nat Rev Mol Cell Biol.* 2021;22:266–82.
- Duan JY, Lin X, Xu F, Shan SK, Guo B, Li FX, et al. Ferroptosis and its potential role in metabolic diseases: a curse or revitalization? *Front Cell Dev Biol.* 2021;9:701788.
- Du L, Wu Y, Fan Z, Li Y, Guo X, Fang Z, et al. The role of ferroptosis in nervous system disorders. *J Integr Neurosci.* 2023;22:19.
- Fang X, Ardehali H, Min J, Wang F. The molecular and metabolic landscape of iron and ferroptosis in cardiovascular disease. *Nat Rev Cardiol.* 2023;20:7–23.
- Ni L, Yuan C, Wu X. Targeting ferroptosis in acute kidney injury. *Cell Death Dis.* 2022;13:182.
- Geng Z, Guo Z, Guo R, Ye R, Zhu W, Yan B. Ferroptosis and traumatic brain injury. *Brain Res Bull.* 2021;172:212–19.
- Sun Y, Chen P, Zhai B, Zhang M, Xiang Y, Fang J, et al. The emerging role of ferroptosis in inflammation. *Biomed Pharmacother.* 2020;127:110108.
- Ouyang S, You J, Zhi C, Li P, Lin X, Tan X, et al. Ferroptosis: the potential value target in atherosclerosis. *Cell Death Dis.* 2021;12:782.
- Du G, Zhang Q, Huang X, Wang Y. Molecular mechanism of ferroptosis and its role in the occurrence and treatment of diabetes. *Front Genet.* 2022;13:1018829.
- Wang Y, Wei Z, Pan K, Li J, Chen Q. The function and mechanism of ferroptosis in cancer. *Apoptosis.* 2020;25:786–98.
- Lei G, Zhuang L, Gan B. Targeting ferroptosis as a vulnerability in cancer. *Nat Rev Cancer.* 2022;22:381–96.
- Liang C, Zhang X, Yang M, Dong X. Recent progress in ferroptosis inducers for cancer therapy. *Adv Mater.* 2019;31:e1904197.
- Smith LM, Kelleher NL. Consortium for Top Down P. Proteoform: a single term describing protein complexity. *Nat Methods.* 2013;10:186–7.
- Nussinov R, Tsai CJ, Xin F, Radivojac P. Allosteric post-translational modification codes. *Trends Biochem Sci.* 2012;37:447–55.
- Hann SR. Role of post-translational modifications in regulating c-Myc proteolysis, transcriptional activity and biological function. *Semin Cancer Biol.* 2006;16:288–302.
- Li Z, Xu X. Post-translational modifications of the mini-chromosome maintenance proteins in DNA replication. *Genes.* 2019;10:331.
- Chatterjee S, Senapati P, Kundu TK. Post-translational modifications of lysine in DNA-damage repair. *Essays Biochem.* 2012;52:93–111.
- Lee JM, Hammaren HM, Savitski MM, Baek SH. Control of protein stability by post-translational modifications. *Nat Commun.* 2023;14:201.
- Sales-Gil R, Vagnarelli P. How HP1 post-translational modifications regulate heterochromatin formation and maintenance. *Cells.* 2020;9:1460.
- Kretova M, Selicky T, Cipakova I, Cipak L. Regulation of pre-mRNA splicing: indispensable role of post-translational modifications of splicing factors. *Life (Basel).* 2023;13:604.
- Cuijpers SAG, Vertegaal ACO. Guiding mitotic progression by crosstalk between post-translational modifications. *Trends Biochem Sci.* 2018;43:251–68.
- Blanc RS, Richard S. Arginine methylation: the coming of age. *Mol Cell.* 2017;65:8–24.
- Karkhanis V, Hu YJ, Baiocchi RA, Imbalzano AN, Sif S. Versatility of PRMT5-induced methylation in growth control and development. *Trends Biochem Sci.* 2011;36:633–41.
- Stopa N, Krebs JE, Shechter D. The PRMT5 arginine methyltransferase: many roles in development, cancer and beyond. *Cell Mol Life Sci.* 2015;72:2041–59.
- Kim H, Ronai ZA. PRMT5 function and targeting in cancer. *Cell Stress.* 2020;4:199–215.
- Abumustafa W, Zamer BA, Khalil BA, Hamad M, Maghazachi AA, Muhammad JS. Protein arginine N-methyltransferase 5 in colorectal carcinoma: Insights into mechanisms of pathogenesis and therapeutic strategies. *Biomed Pharmacother.* 2022;145:112368.
- Zhang D, Tang Z, Huang H, Zhou G, Cui C, Weng Y, et al. Metabolic regulation of gene expression by histone lactylation. *Nature.* 2019;574:575–80.
- Xie Y, Hu H, Liu M, Zhou T, Cheng X, Huang W, et al. The role and mechanism of histone lactylation in health and diseases. *Front Genet.* 2022;13:949252.
- Liu X, Zhang Y, Li W, Zhou X. Lactylation, an emerging hallmark of metabolic reprogramming: Current progress and open challenges. *Front Cell Dev Biol.* 2022;10:972020.
- Wang X, Fan W, Li N, Ma Y, Yao M, Wang G, et al. YY1 lactylation in microglia promotes angiogenesis through transcription activation-mediated upregulation of FGF2. *Genome Biol.* 2023;24:87.
- Motolani A, Martin M, Sun M, Lu T. The structure and functions of PRMT5 in human diseases. *Life (Basel).* 2021;11:1074.
- Yan H, Talty R, Johnson CH. Targeting ferroptosis to treat colorectal cancer. *Trends Cell Biol.* 2023;33:185–88.

34. Murakami S, Jaffrey SR. Hidden codes in mRNA: control of gene expression by m(6)A. *Mol Cell*. 2022;82:2236–51.
35. Qiu L, Jing Q, Li Y, Han J. RNA modification: mechanisms and therapeutic targets. *Mol Biomed*. 2023;4:25.
36. Xin Q, Wang H, Li Q, Liu S, Qu K, Liu C, et al. Lactylation: a passing fad or the future of posttranslational modification. *Inflammation*. 2022;45:1419–29.
37. Liu M, Yao B, Gui T, Guo C, Wu X, Li J, et al. PRMT5-dependent transcriptional repression of c-Myc target genes promotes gastric cancer progression. *Theranostics*. 2020;10:4437–52.
38. Wang Z, Li R, Hou N, Zhang J, Wang T, Fan P, et al. PRMT5 reduces immunotherapy efficacy in triple-negative breast cancer by methylating KEAP1 and inhibiting ferroptosis. *J Immunother Cancer*. 2023;11:e006890.
39. Fan Y, Wang Y, Dan W, Zhang Y, Nie L, Ma Z, et al. PRMT5-mediated arginine methylation stabilizes GPX4 to suppress ferroptosis in cancer. *Nat Cell Biol*. 2025;27:641–53.
40. Wu Y, Wang Z, Han L, Guo Z, Yan B, Guo L, et al. PRMT5 regulates RNA m6A demethylation for doxorubicin sensitivity in breast cancer. *Mol Ther*. 2022;30:2603–17.
41. Meng S, Liu H, Xu J, Deng C, Qian X, Chu S, et al. PRMT5-mediated ALKBH5 methylation promotes colorectal cancer immune evasion via increasing CD276 expression. *Research (Wash D C)*. 2025;8:0549.
42. Qu J, Yan H, Hou Y, Cao W, Liu Y, Zhang E, et al. RNA demethylase ALKBH5 in cancer: from mechanisms to therapeutic potential. *J Hematol Oncol*. 2022;15:8.
43. Zhai J, Chen H, Wong CC, Peng Y, Gou H, Zhang J, et al. ALKBH5 drives immune suppression via targeting AXIN2 to promote colorectal cancer and is a target for boosting immunotherapy. *Gastroenterology*. 2023;165:445–62.
44. Shen D, Lin J, Xie Y, Zhuang Z, Xu G, Peng S, et al. RNA demethylase ALKBH5 promotes colorectal cancer progression by posttranscriptional activation of RAB5A in an m6A-YTHDF2-dependent manner. *Clin Transl Med*. 2023;13:e1279.
45. Luo J, Yu H, Yuan Z, Ye T, Hu B. ALKBH5 decreases SLC7A11 expression by erasing m6A modification and promotes the ferroptosis of colorectal cancer cells. *Clin Transl Oncol*. 2023;25:2265–76.
46. Huang Z, Lin G, Hong Y, Weng L, Zhu K, Zhuang W. High expression of AlkB homolog 5 suppresses the progression of non-small cell lung cancer by facilitating ferroptosis through m6A demethylation of SLC7A11. *Environ Toxicol*. 2024;39:4035–46.
47. Yang P, Wang Q, Liu A, Zhu J, Feng J. ALKBH5 holds prognostic values and inhibits the metastasis of colon cancer. *Pathol Oncol Res*. 2020;26:1615–23.
48. Ge J, Liu SL, Zheng JX, Shi Y, Shao Y, Duan YJ, et al. RNA demethylase ALKBH5 suppresses tumorigenesis via inhibiting proliferation and invasion and promoting CD8(+) T cell infiltration in colorectal cancer. *Transl Oncol*. 2023;34:101683.
49. Zhang Z, Wang L, Zhao L, Wang Q, Yang C, Zhang M, et al. N6-methyladenosine demethylase ALKBH5 suppresses colorectal cancer progression potentially by decreasing PHF20 mRNA methylation. *Clin Transl Med*. 2022;12:e940.
50. Wu X, Dai M, Li J, Cai J, Zuo Z, Ni S, et al. m(6)A demethylase ALKBH5 inhibits cell proliferation and the metastasis of colorectal cancer by regulating the FOXO3/miR-21/SPRY2 axis. *Am J Transl Res*. 2021;13:11209–22.
51. Pan RY, He L, Zhang J, Liu X, Liao Y, Gao J, et al. Positive feedback regulation of microglial glucose metabolism by histone H4 lysine 12 lactylation in Alzheimer's disease. *Cell Metab*. 2022;34:634–48.e6.
52. Yu J, Chai P, Xie M, Ge S, Ruan J, Fan X, et al. Histone lactylation drives oncogenesis by facilitating m(6)A reader protein YTHDF2 expression in ocular melanoma. *Genome Biol*. 2021;22:85.
53. Lv X, Lv Y, Dai X. Lactate, histone lactylation and cancer hallmarks. *Expert Rev Mol Med*. 2023;25:e7.
54. Sun L, Zhang Y, Yang B, Sun S, Zhang P, Luo Z, et al. Lactylation of METTL16 promotes cuproptosis via m(6)A-modification on FDX1 mRNA in gastric cancer. *Nat Commun*. 2023;14:6523.
55. Chen Y, Wu J, Zhai L, Zhang T, Yin H, Gao H, et al. Metabolic regulation of homologous recombination repair by MRE11 lactylation. *Cell*. 2024;187:294–311.e21.
56. Xie B, Zhang M, Li J, Cui J, Zhang P, Liu F, et al. KAT8-catalyzed lactylation promotes eEF1A2-mediated protein synthesis and colorectal carcinogenesis. *Proc Natl Acad Sci USA*. 2024;121:e2314128121.
57. Cheng Z, Huang H, Li M, Chen Y. Proteomic analysis identifies PFKF lactylation in SW480 colon cancer cells. *iScience*. 2024;27:108645.
58. Zhong X, He X, Wang Y, Hu Z, Huang H, Zhao S, et al. Warburg effect in colorectal cancer: the emerging roles in tumor microenvironment and therapeutic implications. *J Hematol Oncol*. 2022;15:160.
59. Li H, Sun L, Gao P, Hu H. Lactylation in cancer: current understanding and challenges. *Cancer Cell*. 2024;42:1803–07.
60. Shen Y, Zhao P, Dong K, Wang J, Li H, Li M, et al. Tadalafil increases the antitumor activity of 5-FU through inhibiting PRMT5-mediated glycolysis and cell proliferation in colorectal cancer. *Cancer Metab*. 2022;10:22.

AUTHOR CONTRIBUTIONS

ML, QD, LY, and SG provided the study concept and design. BY, ZY, and MX wrote the manuscript. SQ, BF, MX, YQ, LM, YJ, FH, JZ, MX, and JH performed the experiments. QZ and XZ interpreted and analyzed the data. YW and WX collected the patients' samples. YJ, SG, BY, and ML provided financial support. ML, QD, LY, and SG is responsible for the overall content as the guarantor and supervised the project. All authors approved the final version of the manuscript.

FUNDING

This work was supported by the Talent Construction Fund Research Project of Jiangsu Province Geriatric Hospital (Grant No. IR2024103), the Research Incubation Startup Fund of Jiangsu Province Geriatric Hospital (Grant No. FHQD202502), the Natural Science Foundation of Jiangsu Province (Grant No. BK202402101, BK20231261, BK20241997, BK20241998), the Jiangsu Primary Research & Development Plan (Grant No. BE2021747) and the Medical scientific research project of Jiangsu Provincial Commission of Health (Grant No. H2023048).

COMPETING INTERESTS

The authors declare no competing interests.

ETHICS APPROVAL AND CONSENT TO PARTICIPATE

Written informed consent was obtained from all patients and the study was approved by the Ethics Committee of Jiangsu Province Geriatric Hospital. Animal experiments were performed according to the Health Guide for the Care and Use of Laboratory Animals approved by the Animal Experimental Research Ethics Committee of Jiangsu Province Geriatric Hospital.

ADDITIONAL INFORMATION

Supplementary information The online version contains supplementary material available at <https://doi.org/10.1038/s41388-025-03457-2>.

Correspondence and requests for materials should be addressed to Ming Liu, Qiantong Dong, Liu Yang or Shouyong Gu.

Reprints and permission information is available at <http://www.nature.com/reprints>

Publisher's note Springer Nature remains neutral with regard to jurisdictional claims in published maps and institutional affiliations.

Springer Nature or its licensor (e.g. a society or other partner) holds exclusive rights to this article under a publishing agreement with the author(s) or other rightsholder(s); author self-archiving of the accepted manuscript version of this article is solely governed by the terms of such publishing agreement and applicable law.